THE ASTROPHYSICAL JOURNAL SUPPLEMENT SERIES, 93:485–518, 1994 August

EMISSION-LINE STUDIES OF YOUNG STARS. IV. THE OPTICAL FORBIDDEN LINES

FRED HAMANN
Department of Astronomy, The Ohio State University; and Center for Astrophysics and Space Sciences, University of California, San Diego, Mail Code 0111, La Jolla, CA 92093-0111; hamann@cass157.ucsd.edu
Received 1993 September 13; accepted 1994 January 20

ABSTRACT

Optical forbidden line strengths and profiles are discussed for a sample of 30 T Tauri stars and 12 Herbig Ae–Be stars. Transitions of [C I], [N II], [O I], [O II], [S II], [Ca II], [Cr II], [Fe II], and [Ni II] are detected. Profile variability occurred in DG Tau and probably other sources. The ensemble profiles can be divided into four generic components that may represent distinct emitting regions; (1) narrow rest-velocity lines, (2) "low"-velocity lines (peaking at $\lesssim \pm 50$ km s^{-1}), (3) "high"-velocity (usually $\gtrsim \pm 100$ km s^{-1}) blueshifted peaks or wings, and (4) high-velocity redshifted peaks. Among T Tauri stars, the rest-velocity lines appear most often in sources with weak and narrow permitted lines, such as the Ca II triplet. The low- and high-velocity blueshifted components usually appear together in sources with strong and broad Ca II triplet lines.

If the velocity-shifted lines form in jets, the smallest (full) opening angles required by the profiles are $\lesssim 20°$ for the narrow, blueshifted [Ca II] lines of DG Tau and HL Tau. Other lines in DG Tau are much broader, implying larger opening angles or greater velocity dispersions. The variability in DG Tau also implies significant changes in the collimation or velocity coherence on timescales of a few years. RW Aur and AS 353A have blue- and redshifted line peaks that could form in oppositely directed jets. The strong [S II] λ6716 and λ6731 lines in RW Aur are exclusively redshifted and require opening angles $\lesssim 60°$.

Measurements of different profiles in the same spectrum show that the physical conditions change with the line-of-sight velocities. The most persistent trends are for more [N II] and [O II] and less [O I] λ5577 flux at high velocities. Constraints on the physical conditions are derived by modeling the emission lines via multilevel ions in "coronal ionization equilibrium." A single temperature and density cannot fully describe the line spectra in any velocity interval. Temperatures in the [O I] region are $9000 \lesssim T_e < 14{,}000$ K, and the ionization fraction (of H) is <35%. The densities derived from [O I] include $n_e \lesssim 5 \times 10^5$ to $\sim 10^7$ cm^{-3}, but $n_e \gtrsim 10^6$ cm^{-3} obtains only at low velocities. In the [S II] regions the densities are lower, $10^3 \lesssim n_e \lesssim 7 \times 10^4$ cm^{-3}, and the temperatures are probably higher, $T_e \gtrsim 13{,}000$ K. At high velocities (only) there is additional hot gas that produces [N II] and [O II], possibly most of the [S II], and little [O I]. This region is characterized by $T_e \gtrsim 15{,}000$ K, $n_e \lesssim 10^5$ cm^{-3}, and an ionization fraction ≳50%. When combined with the spatially segregated emitting regions observed by others by spectral imaging, these results suggest decreasing n_e and increasing T_e away from the star in at least the high velocity gas.

Subject headings: ISM: jets and outflows — line: formation — line: profiles — stars: emission-line, Be — stars: pre–main-sequence

1. INTRODUCTION

In three previous papers we examined the optical permitted emission lines of a sample of 53 T Tauri stars (TTSs; Hamann & Persson 1992b, hereafter PP1) and 32 Herbig Ae–Be stars (Hamann & Persson 1992c, PP2) and discussed the relationships between the line emission and infrared excesses (Hamann & Persson 1992a, PP3). In this paper the optical forbidden lines are examined in a slightly expanded data set. Previous work has shown that the forbidden lines of TTSs are often blueshifted and sometimes double-peaked (Jankovics, Appenzeller, & Krautter 1983; Appenzeller, Jankovics, & Östreicher 1984; Edwards et al. 1987). The blueshifting appears less often among Herbig Ae–Be stars (Finkenzeller 1985) but has been observed in several sources (this work; Hamann & Persson 1989; Hughes et al. 1991). The blueshift is attributed to high-velocity winds whose redshifted (far-side) emission is obscured by circumstellar disks.

Edwards et al. (1987) and Raga (1989) modeled the blueshifted, double-peaked profiles as emission from conical winds with latitude-dependent velocity or density structures. Edwards et al. (1987) also estimated that the characteristic size of the forbidden emission line region (FELR) is ~50 AU. Consideration of the thermal balance in TTS winds led Hartmann & Raymond (1989) to conclude that forbidden emission from such extended regions is not possible without additional heating far from the star. They proposed that the lines form in oblique shocks where the winds impact on flared circumstellar disks. Gomez de Castro & Pudritz (1993) suggest that the forbidden lines form in hydromagnetic shocks above the disks, where bipolar winds driven off the disks are focused by magnetic fields.

All of these models describe the FELR as a single-wind environment—bisected by an opaque disk. In contrast, Kwan & Tademaru (1988) suggest that two distinct emitting regions are responsible for the often double-peaked lines. They attribute the low-velocity peak to a slow-moving wind driven off the disk, and the high-velocity peak to a collimated jet formed near the star. Observations of vastly different profiles in different lines also led Edwards et al. (1989) to conclude that there are

multiple emitting regions. They found, for example, that [N II] λ6583 has mostly high-velocity emission, while [O I] λ5577 peaks only at low velocities. They attribute these tendencies to typically lower densities at high velocity.

High-resolution spectral imaging of DG Tau and HL Tau (Solf 1989; Solf & Böhm 1993; Kepner et al. 1993; Mundt, Brugel, & Bührke 1987; Mundt et al. 1990) also indicates multicomponent winds. Those observations show that the low-velocity gas is essentially coincident with the star, while the high-velocity emission is displaced along the direction of extended jets (Mundt & Fried 1983; Mundt et al. 1987). The displacement at high velocities is larger in [S II] and [N II] than in [O I] λ6300, and the line velocities are comparable to those measured in the extended jets (also Edwards et al. 1989). Therefore the high-velocity emission is probably associated with the jets, and the larger displacement of [S II] and [N II] suggests decreasing densities away from the star.

The present paper uses the forbidden-line strengths and profiles to help delineate the emitting regions and estimate their physical conditions. The analysis of the line ratios uses the spectral synthesis code CLOUDY (Ferland 1993) with the assumptions of "coronal ionization equilibrium" and multilevel ions in detailed balance. The theoretical predictions are given in an Appendix. The observations are described in § 2. The results are presented in § 3 in the form of tabulated line strengths (§ 3.1), plotted line profiles (§ 3.2), and notes on some individual sources (§ 3.3). Section 4 discusses the constraints implied by the data for the kinematics and morphology of the FELR (§§ 4.1 and 4.2), and for the densities, temperatures, and ionizations (§ 4.3). The results are summarized in § 5.

2. OBSERVATIONS AND DATA REDUCTION

Spectra were obtained at the Palomar, Las Campanas, and Kitt Peak National Observatories using different instruments, resolutions, and wavelength coverages (between ~3800 and ~9500 Å). Some sources were observed more than once to test for variability and expand the wavelength coverage. Table 1 (§ 3.1 below) lists the observing parameters for the sources with forbidden line detections. Complete logs of those observations between 1983 and 1989 are given in PP1 and PP2. Additional spectra were obtained in 1990 February and October with the echelle spectrometer on the 1.5 m telescope at Palomar Observatory, and in 1990 April with the modular spectrograph on the 2.5 m telescope at Las Campanas. Most of the sources observed at Las Campanas in 1989 April (see Table 1) were measured twice; once with the modular spectrograph in an echelle mode to obtain spectra from ~6125 to ~9180 Å and again 1–5 days later with the two-dimensional Frutti echelle to measure ~3800 to ~7000 Å.

The data were reduced using standard techniques with the IRAF[1] software. Spectra were extracted across only the $\lesssim 1''.5$ diameter seeing disk of the stars. No attempt was made to measure more extended emission. Telluric emission lines, e.g., of [O I], were removed by subtracting spectra of the night sky. The sky spectra were measured in the same exposure as the sources, except for the Palomar 1.5 m (1990) and the Las Campanas 2.5 m short-wavelength (1989) observations, where the limited slit length required separate sky exposures. Those were obtained immediately after or between the source integrations except as noted in § 3.3. Wavelength calibration was achieved by measuring arc lamps at each telescope position. None of the spectra are flux-calibrated. They are instead normalized to unity by fitting a low-order polynomial to the continua. Line flux ratios are estimated by scaling the equivalent widths according to an extinction-corrected continuum derived from previous broadband photometry. The extinctions and photometry are tabulated in PP3, except for DK Tau, which is taken from Basri & Bertout (1989). The extinction toward RW Aur is unknown, so none is included.

A few of the forbidden lines are contaminated by weak telluric absorptions. These absorptions were removed by division using early-type standard stars observed the same night at comparable airmass. Because the division adds noise to the source spectra, the ratioed data are used only at wavelengths clearly containing telluric features: ~6275 to ~6320 Å, ~7170 to ~7320 Å, ~8130 to ~8370 Å, and beyond ~8950 Å. No attempt was made to remove underlying photospheric absorptions in the stars themselves.

Inspection of the 1990 October spectra shows that spurious emission sometimes appears at wavelengths near [S II] 6731 Å. This pseudoemission is caused by a cluster of "cold" pixels that were not properly scaled by the flat-field division. The 6731 Å detections in that data set are therefore considered dubious unless corroborating [S II] lines are present. The questionable detections are listed as "[S II]?" in Table 1. Finally, [O I] λ6364 was sometimes not detected in the 1983 December data because of poor sensitivity at that edge of the wavelength coverage.

3. RESULTS

3.1. *Forbidden-Line Strengths and Detections*

Table 1 lists the sources for which at least one forbidden line is detected. This includes 30 of 53 TTSs and 12 of 32 Herbig Ae–Be stars. Any source listed in PP1 or PP2 but not appearing in Table 1 did not have a forbidden line within the wavelength coverage. The only other source observed with no detectable forbidden lines is LkCa 18, which was measured in 1990 October from ~3660 to ~9450 Å with the 1.5 m echelle at Palomar. The stars are numbered in Table 1 (first column) as in PP1, PP2, and PP3, i.e., organized by observing run and divided between TTSs and Herbig Ae–Be stars. The Herbig stars have numbers 61 or larger. Table 1 also lists the spectral coverage (second column), the resolution (third column), and the dates of the observations (fourth column). The 1989 April spectra often have a gap in the wavelength coverage from ~6950 to ~7250 Å due to a bad column on the CCD. This wavelength gap includes [Fe II] 7155 and 7172 Å. The 1988 February spectra have bad columns effecting the entire region between ~6800 and ~7550 Å. This contaminated region overlaps with [Ca II], [Ni II], and several of the [Fe II] lines (see below and Table 1 notes). Table 1 also lists the forbidden lines detected in each object (fifth column). Lines searched for but not detected in any object include the [N I] ~5200 Å doublet, [N II] λ5755, [O III] λ5007, [S III] λ9069, and [Ar III] λ7136.

[1] The IRAF software is distributed by the National Optical Astronomy Observatories under contract with the National Science Foundation.

TABLE 1

FORBIDDEN LINE MEASUREMENTS

Source	wavelength range (Å)	resolution (km s^{-1})	obs. date	lines detected[1]	notes[2]
1. TW Cha	6125–9180	35	Apr. 89	[O I]	nw,1p, $W_\lambda(6300) \approx 0.95$Å, FWHM(6300) < 43 km s^{-1}
2. LkHα 332-20	3800–7000	11	Apr. 89	[O I]	nw,1p, $W_\lambda(6300) \sim 0.08$Å
	6125–9180	35	"		
3. VW Cha	3800–7000	11	Apr. 89	[O I]	br,2p?, $W_\lambda(6300) \approx 0.93$Å
	6125–9180	35	"		
4. VZ Cha	3800–7000	11	Apr. 89	[O I]	nw,1p, $W_\lambda(6300) \approx 0.42$Å, FWHM(6300) < 42 km s^{-1}
	6125–9180	35	"		
5. CV Cha	3800–7000	11	Apr. 89	[O I]	nw,1p, $W_\lambda(6300) \approx 0.14$Å
	6125–9180	35	"		
6. HM 32	3800–7000	11	Apr. 89	[O I],[S II]	nw,1p,cx? $W_\lambda(6300) \approx 1.40$Å, FWHM(6300) $\lesssim 15$ km s^{-1}
	6125–9180	35	"		$V_* \approx 14.8$ km s^{-1}
7. SZ 68	3800–7000	11	Apr. 89	[O I]?	nw,1p, $W_\lambda(6300) \lesssim 0.03$Å
	6125–9180	35	"		
8. HM Lup	3800–7000	11	Apr. 89	[O I],[S II]	br,blu,cx, $W_\lambda(6300) \approx 0.90$Å
	6125–9180	35	"		$V_* \approx 0.0$ km s^{-1}
9. GQ Lup	3800–7000	11	Apr. 89	[O I]	nw,1p?, $W_\lambda(6300) \sim 0.08$Å,
	6125–9180	35	"		FWHM(6300) $\lesssim 40$ km s^{-1}
10. RU Lup	3800–7000	11	Apr. 89	[N II],[O I],	br,blu,cx, $W_\lambda(6300) \approx 1.94$Å
	6125–9180	35	"	[S II],[Fe II]	$V_* \approx 2.1$ km s^{-1}
	6470–9240	37	Feb. 88		
11. AS 205	3800–7000	11	Apr. 89	[O I],[S II],	2p,blu, $W_\lambda(6300) \approx 1.16$Å,
	6125–9180	35	"	[N II]?	$V_* \approx -2.1$ km s^{-1}
	6470–9240	37	Feb. 88		
12. Haro 1-1	3800–7000	11	Apr. 89	[O I],[S II]	nw,1p, $W_\lambda(6300) \approx 0.52$Å,
	6125–9180	35	"		FWHM(6300) $\lesssim 40$ km s^{-1}
	6470–9240	37	Feb. 88		
13. SR 9	3800–7000	11	Apr. 89	[O I]	nw,1p, $W_\lambda(6300) \sim 0.06$Å
	6125–9180	35	"		
	7550–9280	22	June 87		
14. S CrA	3800–7000	11	Apr. 89	[O I],[S II],	br,blu,cx, $W_\lambda(6300) \approx 2.31$Å
	6125–9180	35	"	[Fe II]	$V_* \approx 4.6$ km s^{-1}
	7550–9280	22	June 87		
15. VV CrA	4825–9720	65	Apr. 90	[N II],[O I],[O II],[S II],	br,blu,cx, $W_\lambda(6300) \approx 9.06$Å
	6125–9180	35	Apr. 89	[Ca II],[Fe II],[Ni II]	$V_* \approx -1.4$ km s^{-1}
16. AS 353A	3800–7000	11	Apr. 89	[O I],[S II],	br,blu,red,cx, $W_\lambda(6300) \approx 1.34$Å
	6125–9180	35	"	[Ca II],[Fe II]	$V_* \approx -6.6$ km s^{-1}
	7550–9280	22	June 87		
17. V536 Aql	6125–9180	35	Apr. 89	[C I]?,[N II],[O I],	br,blu,cx, $W_\lambda(6300) \approx 10.3$Å
	3870–4090	70	Sep. 88	[O II],[S II],[Fe II]	$V_* \approx -7.8$ km s^{-1}
	8330–8970	60	"		
18. CW Tau	3660–9900	19	Feb. 90	[N II],[O I],	br,blu,cx, $W_\lambda(6300) \approx 6.96$Å
	3870–4090	70	Nov. 88	[S II],[Fe II]	$V_* \approx 20.6$ km s^{-1}
	8330–8970	60	"		
27. WL 22	3870–4090	70	Sep. 88	[Fe II]	br,blu,2p, $W_\lambda(8617) \approx 0.88$Å
	8330–8970	60	"		
28. V1331 Cyg	3870–4090	70	Sep. 88	[S II],[Fe II]	br,blu,1p, $W_\lambda(8617) \approx 1.10$Å
	8330–8970	60	"		
34. CT Cha	6470–9240	37	Feb. 88	[S II]	br,1p, $W_\lambda(6731) \approx 0.31$Å, FWHM(6731) ≈ 75 km s^{-1}
35. WW Cha	6470–9240	37	Feb. 88	[S II]	br?,1p, $W_\lambda(6731) \sim 0.10$Å

TABLE 1—*Continued*

Source	wavelength range (Å)	resolution (km s^{-1})	obs. date	lines detected[1]	notes[2]
42. RY Tau	3660–9450	19	Oct. 90	[O I],[S II]?,	br,blu,cx, $W_\lambda(6300) \approx 0.40$Å
	7280–9100	22	Dec. 87	[Fe II]	$V_* \approx 16.4$ km s^{-1}
44. DF Tau	3660–9450	19	Oct. 90	[O I]	br,blu,cx, $W_\lambda(6300) \approx 1.88$Å
	7280–9100	22	Dec. 87		$V_* \approx 17.6$ km s^{-1}
45. DG Tau	3660–9900	19	Feb. 90	[N II],[O I],[O II],[S II],	br,blu,cx,v, $W_\lambda(6300) \approx 7.43$Å
	7280–9100	22	Dec. 87	[Ca II],[Fe II],[Ni II]	$V_* \approx 20.0$ km s^{-1}
46. HL Tau	7280–9100	22	Dec. 87	[N II],[O I],[S II],	br,blu,cx, $W_\lambda(6731) \approx 2.01$Å
	6320–6900	85	Dec. 83	[Ca II],[Fe II],[Ni II]	
47. XZ Tau	7340–9100	22	Dec. 87	[N II],[O I],[S II]	br?,blu,cx, $W_\lambda(6731) \approx 7.02$Å
	6320–6900	85	Dec. 83		
49. RW Aur	3660–9900	19	Feb. 90	[O I],[S II],	br,blu,red,cx, $W_\lambda(6300) \approx 1.09$Å
	7280–9100	22	Dec. 87	[Ca II],[Fe II]	$V_* \approx 16.0$ km s^{-1}
54. BP Tau	3660–9450	19	Oct. 90	[O I]	1p, $W_\lambda(6300) \approx 0.21$Å
55. DK Tau	3660–9450	19	Oct. 90	[O I],[S II]	br,blu,cx, $W_\lambda(6300) \approx 1.15$Å
					$V_* \approx 15.3$ km s^{-1}
61. V380 Ori	3660–9900	19	Feb. 90	[O I],[Ca II],	br,1p,blu? $W_\lambda(6300) \approx 0.25$Å,
	3800–7000	11	Apr. 89	[Fe II]	FWHM(6300) ≈ 75 km s^{-1}
	6125–9180	35	Apr. 89		
	7280–9100	22	Dec. 87		
62. Z CMa	3800–7000	11	Apr. 89	[O I],[S II],	br,1p, $W_\lambda(7291) \sim 0.22$Å,
	6125–9180	35	"	[Ca II],[Fe II]	FWHM(7291) ≈ 53 km s^{-1}
	7280–9100	22	Dec. 87		
	6320–6900	85	Dec. 83		
63. HD 97048	3800–7000	11	Apr. 89	[O I]	nw,1p,$W_\lambda(6300) \approx 0.18$Å,
	6125–9180	35	"		FWHM(6300) < 40 km s^{-1}
65. KK Oph	3800–7000	11	Apr. 89	[C I],[N II],[O I],	br,cx, $W_\lambda(6300) \approx 1.75$Å,
	6125–9180	35	"	[O II],[S II],[Ca II],	FWHM(6300) ≈ 73 km s^{-1}
	7550–9280	22	June 87	[Fe II],[Ni II]	
66. R CrA	3800–7000	11	Apr. 89	[N II],[O I],[S II],	br,blu?,cx?, $W_\lambda(6300) \approx 2.01$Å
	6125–9180	35	"	[Fe II],[Ni II]	
	7550–9280	22	June 87		
68. LkHα 348	3870–4090	70	Sep. 88	[S II]?,[Fe II]	nw,1p, $W_\lambda(8617) \approx 0.19$Å,
	7262–7909	80	"		FWHM(8617) < 60 km s^{-1}
	8330–8970	60	"		
69. PV Cep	8330–8970	60	Sep. 88	[Fe II]	br,blu,cx, $W_\lambda(8617) \approx 6.80$Å
70. LkHα 233	3870–4090	70	Sep. 88	[Fe II]	nw,blu,1p, $W_\lambda(8617) \approx 0.22$Å
	8330–8970	60	"		
72. AB Aur	3660–9900	19	Feb. 90	[O I]	nw,1p, $W_\lambda(6300) \approx 0.11$Å,
	7280–9100	22	Dec. 87		FWHM(6300) < 39 km s^{-1}
73. HK Ori	7340–9100	22	Dec. 87	[Cr II],[Fe II],[Ni II]	br,1p, $W_\lambda(7378) \approx 0.75$Å,
					FWHM(7378) ≈ 65 km s^{-1}
77. HD 259431	7280–9100	22	Dec. 87	[O I]	br,1p, $W_\lambda(6364) \sim 0.22$Å,
	6320–6900	85	Dec. 83		FWHM(6364) ~ 160 km s^{-1}
78. R Mon	7280–9100	22	Dec. 87	[N II]?,[O I],[S II],[Ca II]?,	br,blu,cx, $W_\lambda(6731) \approx 1.43$Å
	6320–6900	85	Dec. 83	[Cr II],[Fe II],[Ni II]	

[1] [C I] = 8727 Å; [N II] = 6548 or 6583 Å; [O I] = 5577, 6300, or 6364 Å; [O II] = 7319 and 7330 Å; [S II] = 4069, 4076, 6716, or 6731 Å; [S II] = 4069, 4076, 6716, or 6731 Å; [Ca II] = 7291 or 7324 Å; [Cr II] = 8000, 8125 Å, or others; [Fe II] = 4244, 4815, 5262, 7155, 7388, 7452, 8617, 8892 Å, or others; [Ni II] = 7378, 7412 Å, or others.

[2] Abbreviations: nw = narrow profile(s) (unresolved for FWHM $\lesssim 40$ km s^{-1}); br = broad profile(s) (resolved with FWHM > 40 km s^{-1}); blu = blueshifted line centroid(s) or peak(s); red = redshifted line centroid(s) or peak(s); 1p = single-peaked profile(s); 2p = double-peaked profile(s); cx = complex profile(s)—more than two peaks, strong asymmetries, or different profiles in different lines; v = variable profile(s).

The detection of [N I] ~5200 Å is often made difficult by emission from Fe II (49) 5197.6 Å.

Finally, Table 1 contains notes on the line strengths and profiles, and on the stellar radial velocities (sixth column). The stellar velocities, V_*, were measured from the centroid of the Li I (1) 6707.81 Å photospheric absorption for sources plotted in the figures below. The 1 σ uncertainties in V_* are typically ± 2 km s^{-1}. The equivalent widths (W_λ) are listed for [O I] λ6300 or for the strongest measured forbidden line. These measurements should supersede any prior listings in PP1 or PP2 (from the same data) because that work did not always take full account of the broad wings or multiple line peaks. The full width at half-maximum (FWHM) of the strongest line is also given, *if* its profile is roughly symmetric about the rest velocity. Sources with complex or multipeaked profiles are shown in the figures. In some cases the FWHM could not be measured because of severe blending with photospheric absorption lines (e.g., LkHα 332-20, CV Cha, Sz 68, and SR 9). In others the FWHM is only an upper limit (VZ Cha, HM 32) because the measured width is not much larger than the resolution. For repeated observations at the same wavelength, e.g., in 1989 April at [O I] 6300 Å, the highest resolution data was used to measure the FWHM if there was a sufficiently large signal-to-noise ratio.

Tables 2–5 list representative forbidden-line strengths for several sources. The lists in Tables 2–4 are not always complete, but Table 5 is a complete list of all forbidden lines detected in the 1989 April spectra of KK Oph. In Table 2, the complex line profiles of several sources are divided into "high" and "low" velocity bins so that the flux in these intervals can be studied separately (§ 4.2.1). The dividing velocities, V_0, in the stellar rest frame are given next to the source names. These are used for the measurements of every line in each source. The velocities are defined by the position of minimum flux between the peaks in multipeaked lines. The only exception is S CrA where an arbitrary division was made between the blueshifted peaks and the redward wings (see § 4.2.1). For each source Table 2 lists the line identifications, and the equivalent widths for the "high" velocity side, "low" velocity side, and total line. Extinction-corrected fluxes for the "high," "low," and total are given relative to [O I] λ6300 or for the strongest line measured. The line identifications use the Moore (1972) multiplet numbers. Laboratory wavelengths (more important for the profile plots below) are from Johansson (1977), Moore (1972), or the energy level tables of Bashkin & Stoner (1978). Table 3 lists the strengths of the multipeaked profiles of AS 353A and RW Aur in three velocity bins: "blue," "center," and "red." The dividing velocities, again listed next to the source names, are roughly coincident with the minima in the multipeaked [O I] λ6300 profiles. Tables 4 and 5 provide total (only) line strengths for several additional sources. Blended features in Table 5 are measured together, such as λ4358 and λ4359, with the equivalent widths and fluxes recorded next to the first member of the blend (e.g., λ4358). The equivalent width column of the second member (λ4359) notes that this line is blended with the feature above it.

3.2. *Forbidden-Line Profiles*

Figures 1 and 2 plot representative forbidden-line profiles for several TTSs and Herbig Ae–Be stars, respectively. The same lines are plotted twice for some of the 1989 April data to confirm the profiles and compare the results at different resolutions. The profiles observed with the short-wavelength echelle can be distinguished by their smaller pixel widths and larger pixel-to-pixel fluctuations. The velocities in the figures and throughout this paper are relative to the stellar velocities in Table 1, unless noted otherwise. The figures also show the Li I λ6708 absorption line if it is detected. If it is not, narrow permitted emission lines are plotted for velocity reference. The two [O II] "lines" are actually close pairs with wavelengths 7318.6 and 7319.7 Å, and 7329.9 and 7331.0 Å (Bashkin & Stoner 1978). These lines are plotted assuming mean wavelengths of 7319.2 and 7330.5 Å based on the comparable transition strengths of the components (Seaton & Osterbrock 1957).

3.3. *Notes on Some Individual Sources*

HM 32.—The narrow [O I] lines are not due to sky emission. They have the same equivalent width in both the long- and short-wavelength spectra from 1989 April, even though different methods of sky subtraction were used in the data reduction (§ 2). The [S II] λ4069 profile is noisy but appears broader than the [O I].

HM Lup.—The profiles have poor signal-to-noise ratio, but the ensemble [O I] and [S II] measurements reveal distinct high- and low-velocity peaks. The small apparent redshift in the [O I] peaks in the long-wavelength spectrum of 1989 April is not corroborated by λ6300 in the short-wavelength spectrum. [S II] λ6716 and λ4076 are not detected.

RU Lup.—There is no evidence for variability between the 1988 February and 1989 April observations. The weak [N II] line is present in both spectra. The profiles differ dramatically between lines. The main peaks are at roughly -15 km s^{-1} and -140 km s^{-1}.

AS 205.—The blueshifted peak at -225 km s^{-1} in [O I] λ6300 stands well above the noise and is confirmed by its presence in both spectra of 1989 April. [N II] λ6583 may be present, but is listed as an upper limit in Table 2.

S CrA.—All of the forbidden lines have sharp peaks near -120 km s^{-1} and decline sharply at higher negative velocities. The profiles differ significantly in their relative flux at lower velocities. The [N II] lines are not detected.

V V CrA.—The centroids of the forbidden lines are all blueshifted but the profiles differ greatly. The [N II] lines are sharply peaked at -175 km s^{-1} with little emission below -100 km s^{-1}. The [S II] lines have two sharp peaks, one coincident with [N II] and another at -10 km s^{-1}. [O I] λ6300 has comparable flux between roughly -180 and 0 km s^{-1}, and significant wings from -360 km s^{-1} to at least $+150$ km s^{-1}. The [O II] lines at ~7319 and ~7330 Å are present, but they are lesser contributors to the broad blend at these wavelengths. Unlike V536 Aql and DG Tau (below), most of the emission in the blend is due to [Ca II] 7324 Å and Fe II (73) 7308, 7310, and 7321 Å (see notes on DG Tau). The flux attributable to [O II] appears exclusively blueshifted, with velocities comparable to the [N II]. The [O II] measurements in Table 2 attempt to deblend this contribution. There are no significant changes in the forbidden-line profiles between 1989 April and 1990 April, and the [O I] λ6300 equivalent width (used for normalization in Table 2) increased by only ~17%. The [S II] profiles do not

TABLE 2

"HIGH" AND "LOW" VELOCITY FORBIDDEN LINE STRENGTHS[1]

Line ID	W_λ (Å) "high"	W_λ (Å) "low"	W_λ (Å) total	Rel. Flux "high"	Rel. Flux "low"	Rel. Flux total
RU Lup (1989, $V_o \approx -95$ km s^{-1})						
[N II] (3F) 5755	<0.06	<0.06	<0.12	<0.07	<0.05	<0.06
[N II] (1F) 6583	0.18	0.04::	0.28:	0.23	0.03::	0.14:
[O I] (3F) 5577	<0.03	0.09	0.09	<0.04	0.07	0.04
[O I] (1F) 6300	0.79	1.15	1.94	1.00	1.00	1.00
[S II] (1F) 4069	0.51	0.69	1.20	0.87	0.80	0.83
[S II] (2F) 6716	0.08:	0.13::	0.21::	0.10:	0.11::	0.11::
[S II] (2F) 6731	0.19	0.42	0.61	0.24	0.36	0.31
[Fe II] (14F) 7452	0.08:	<0.03	0.08:	0.09:	<0.02	0.04:
AS 205 (1989, $V_o \approx -115$ km s^{-1})						
[N II] (1F) 6583	<0.17	<0.07	<0.23	<0.53	<0.08	<0.19
[O I] (3F) 5577	<0.06	0.15:	0.21:	<0.21	0.19:	0.19:
[O I] (1F) 6300	0.31	0.88	1.19	1.00	1.00	1.00
[S II] (1F) 4068	?	0.21:	0.21:	?	0.44:	0.32:
[S II] (2F) 6731	<0.05	<0.06	<0.09	<0.15	<0.06	<0.07
S CrA (1989, $V_o \approx -55$ km s^{-1})						
[N II] (1F) 6583	<0.03	<0.04	<0.07	<0.02	<0.05	<0.03
[O I] (3F) 5577	<0.05	<0.06	<0.11	<0.04	<0.06	<0.05
[O I] (1F) 6300	1.43	0.88	2.31	1.00	1.00	1.00
[S II] (1F) 4069	0.55	0.12	0.67	0.35	0.13	0.27
[S II] (2F) 6716	0.21	0.06	0.27	0.15	0.07	0.12
[S II] (2F) 6731	0.44	0.14	0.58	0.31	0.16	0.25
[Fe II] (14F) 7155	0.15	0.17	0.33	0.11	0.20	0.14
[Fe II] (14F) 7452	0.07	0.08:	0.15:	0.05	0.09:	0.07:
[Fe II] (13F) 8617	0.13	0.09:	0.22:	0.09	0.10:	0.09:
VV CrA (1989+1990, $V_o \approx -95$ km s^{-1})[2]						
[N II] (3F) 5755	<0.14	<0.14	<0.28	<0.02	<0.03	<0.03
[N II] (1F) 6583	0.39	0.05::	0.44:	0.08	0.01::	0.05:
[O I] (3F) 5577	<0.24	<0.39	<0.63	<0.04	<0.08	<0.06
[O I] (1F) 6300	5.14	4.12	9.06	1.00	1.00	1.00
[O II] (2F) 7319	0.29::	?	0.29::	0.06::	?	0.04::
[O II] (2F) 7330	0.22::	<0.09	0.22::	0.05::	<0.02	0.03::
[S II] (2F) 6716	0.25	0.27	0.52	0.05	0.07	0.06
[S II] (2F) 6731	0.59	0.65	1.24	0.12	0.17	0.14
[Ca II] (1F) 7291	0.41	0.46	0.87	0.09	0.12	0.11
[Fe II] (14F) 7155	1.08	0.51	1.59	0.23	0.13	0.19
[Fe II] (14F) 7452	0.56	0.37	0.93	0.12	0.10	0.11
[Fe II] (13F) 8617	1.00	0.47	1.47	0.21	0.12	0.17
[Ni II] (1F) 7378	0.38	0.22	0.60	0.08	0.06	0.07
[Ni II] (1F) 7412	<0.08	<0.10	<0.18	<0.02	<0.03	<0.02
DF Tau (1990, $V_o \approx -60$ km s^{-1})						
[N II] (1F) 6583	<0.05	<0.05	<0.10	<0.05	<0.05	<0.06
[O I] (3F) 5577	<0.05	0.35	0.35	<0.04	0.33	0.16
[O I] (1F) 6300	0.97	0.91	1.88	1.00	1.00	1.00
[S II] (2F) 6731	<0.08	<0.07	<0.15	<0.09	<0.08	<0.09
DG Tau (1990, $V_o \approx -135$ km s^{-1})						
[N II] (3F) 5755	<0.13	<0.13	<0.26	<0.04	<0.02	<0.03
[N II] (1F) 6583	0.59	0.16:	0.75	0.23	0.03	0.10
[O I] (3F) 5577	<0.08	0.40:	0.40:	<0.03	0.07:	0.04:
[O I] (1F) 6300	2.65	4.78	7.43	1.00	1.00	1.00
[O II] (2F) 7319	0.61::	?	0.61::	0.25::	?	0.09::
[O II] (2F) 7330	0.56::	<0.10	0.66::	0.23::	<0.02	0.10::
[S II] (1F) 4069	?	3.23:	>3.23	?	0.49:	>0.32
[S II] (1F) 4076	?	0.98:	>0.98	?	0.15:	>0.10
[S II] (2F) 6716	0.21	0.65	0.86	0.08	0.14	0.12
[S II] (2F) 6731	0.38	1.36	1.74	0.15	0.30	0.25
[Ca II] (1F) 7291	0.36	0.27	0.63	0.15	0.06	0.09
[Fe II] (14F) 7155	0.60	0.92	1.52	0.24	0.21	0.22
[Fe II] (14F) 7452	0.33:	0.41	0.74	0.14:	0.09	0.11
[Fe II] (13F) 8617	0.28:	0.53	0.81	0.12:	0.12	0.12
[Ni II] (1F) 7378	0.21::	0.24:	0.45::	0.09::	0.06:	0.07::
[Ni II] (1F) 7412	pres.	pres.	pres.	—	—	—
DG Tau (1987, $V_o \approx -135$ km s^{-1})						
[O II] (2F) 7319	2.22:	?	2.22:	1.66:	?	0.78:
[O II] (2F) 7330	2.31:	0.24:	2.55:	1.73:	0.16:	0.90:
[Ca II] (1F) 7291	0.69	0.15::	0.84:	0.52	0.10::	0.30:
[Ca II] (1F) 7324	0.42:	?	0.42:	0.31:	?	0.15:
[Fe II] (14F) 7452	0.83	0.90	1.73	0.63	0.61	0.62
[Fe II] (13F) 8617	1.30	1.46	2.76	1.00	1.00	1.00
[Ni II] (1F) 7378	0.83	0.79	1.62	0.62	0.53	0.57
[Ni II] (1F) 7412	0.35::	0.10::	0.45::	0.26::	0.07::	0.16::
HL Tau (1983+1987, $V_o \approx -85$ km s^{-1})						
[N II] (1F) 6583	1.01	0.17::	1.18:	0.77	0.26::	0.60:
[S II] (2F) 6716	1.12	0.43	1.55	0.80	0.64	0.78
[S II] (2F) 6731	1.34	0.67	2.01	1.00	1.00	1.00
[Ca II] (1F) 7291	0.68	<0.07	0.68	0.45	<0.09	0.30
[Ca II] (1F) 7324	0.31	<0.10	0.31	0.21	<0.13	0.14
[Fe II] (14F) 7388	0.09:	<0.07	0.09:	0.06:	<0.09	0.04:
[Fe II] (13F) 8617	0.41:	<0.10	0.41:	0.22:	<0.11	0.15:
[Ni II] (1F) 7378	0.16:	<0.07	0.16:	0.11:	<0.09	0.07:
DK Tau (1990, $V_o \approx -60$ km s^{-1})						
[N II] (1F) 6583	<0.05	<0.05	<0.10	<0.12	<0.07	<0.09
[O I] (3F) 5577	<0.15	0.44:	0.44:	<0.29	0.47:	0.30:
[O I] (1F) 6300	0.43	0.77	1.20	1.00	1.00	1.00
[S II] (2F) 6731	0.08	0.09	0.17	0.20	0.12	0.15

[1] The line profiles are divided into "high" and "low" velocity bins at V_0 ((in the stellar rest frame) listed next to the object names.
[2] Upper limits on [O I] λ5577 and [N II] λ5577 are from 1990. All other measurements are from 1989.

TABLE 3

AS 353A AND RW AUR FORBIDDEN LINE STRENGTHS[a]

Line ID	W_λ (Å) "blue"	W_λ (Å) "center"	W_λ (Å) "red"	W_λ (Å) total	Rel. Flux "blue"	Rel. Flux "center"	Rel. Flux "red"	Rel. Flux total
AS 353A (1989, $V_o \approx -175, +140$ km s^{-1})								
[O I] (3F) 5577	<0.06	0.13::	<0.06	0.13::	<0.15	0.21::	<0.22	0.10::
[O I] (1F) 6300	0.41	0.65	0.28	1.34	1.00	1.00	1.00	1.00
[S II] (2F) 6731	<0.08	<0.05	<0.05	<0.18	<0.19	<0.08	<0.18	<0.13
[Ca II] (1F) 7291	<0.08	0.36	<0.06	0.36:	<0.19	0.54:	<0.21	0.26:
RW Aur (1990, $V_o \approx -70, +45$ km s^{-1})								
[N II] (1F) 6583	<0.11	<0.08	<0.07	<0.26	<0.34	<0.18	<0.14	<0.20
[O I] (1F) 6300	0.31	0.42	0.47	1.20	1.00	1.00	1.00	1.00
[S II] (1F) 4069	?	0.51	0.83	>1.34	?	1.59	2.31	>1.46
[S II] (2F) 6716	<0.04	<0.03	0.19	0.19	<0.12	<0.07	0.39	0.15
[S II] (2F) 6731	<0.04	<0.03	0.28	0.28	<0.12	<0.07	0.57	0.22
[Ca II] (1F) 7291	0.35	0.42	0.47	1.24	0.92	0.82	0.82	0.85
[Fe II] (14F) 7155	0.26:	0.13	0.19	0.58:	0.71:	0.26	0.34	0.41:
[Fe II] (13F) 8617	0.22:	0.04::	0.19::	0.45::	0.48:	0.06::	0.27::	0.25::

[a] The profiles are divided into "blue," "center," and 'red" bins at the stellar rest frame velocities V_0 listed next to the object names.

appear significantly different from the lower signal-to-noise profiles published by Appenzeller et al. (1984).

AS 353A.—The multiple peaks between ±300 km s^{-1} in the [O I] λ6300 plot are all due to [O I]. The complex profile is confirmed by its appearance in both 1989 spectra and by the similar profile of [O I] λ6364—although λ6364 is blended with weak emission from Fe II (40) 6369.4 Å (at +260 km s^{-1}), Fe I (13) 6353.8 and 6358.7 Å (at −475 and −245 km s^{-1}, respectively), and broad shallow P Cygni–shaped lines of Si II (2) 6347.1 and 6371.4 Å (at −790 and +355 km s^{-1}, respectively). Eislöffel, Solf, & Böhm (1990) did not report the complex profile of [O I] λ6300 in their measurement of this line, but they noted that [O I] λ5577 was twice as strong as λ6300. This is not the case in the present data (Table 3). There is evidence for a multipeak profile in [S II] λ4069, similar to λ6300, although in this case the blue side is overwhelmed by Fe I (43) 4063.6 Å at −370 km s^{-1}. There might also be some contribution to λ4069 from Fe I (43) 4071.7 Å at +220 km s^{-1}. Multipeaked emission may be present in the weak [Fe II] λ8617 line measured in 1989 and 1987. The [Ca II] lines are dominated by broad emission near the stellar rest velocity. This emission was mistakenly not reported in PP1.

V 536 Aql.—In 1989 April the forbidden lines were all blueshifted, but the [N II] peaks were at −80 km s^{-1} compared to only −10 km s^{-1} for [O I] and [S II] λ6731. In 1988 September the [S II] λ4069 and [Fe II] λ8617 profiles were shifted to velocities like the [N II] lines of 1989 April. The disparity among the [S II] lines could be due to variability, but it could also result from intrinsic differences in λ6731 and λ4069 emission regions (§ 4). The latter hypothesis is supported by the lack of variability in [S II] λ6716 and λ6731 between the measurements of 1989 April and those of Appenzeller et al. (1984) in 1983 July. The [C I] detection (Table 4) is marginal.

The [O II] lines in V536 Aql appear blueshifted with velocities comparable to the [N II] peak. They are part of a broad blend between ~7313 and ~7331 Å. If the [O II] profiles are like the other forbidden lines, they cannot account for the entire blend. There remains unaccounted for emission between ~7319 and ~7325 Å. This emission is not due to [Ca II] λ7324 because [Ca II] λ7291 is not present. It is also not due to Fe II (73), as discussed for DG Tau below, because the lines of this multiplet are very weak or absent. The unaccounted for flux is not included in the [O II] measurements in Table 4.

CW Tau.—The strong narrow spikes in the [O I] lines do not match the velocities of the peaks in the other lines and do not appear in the [O I] λ6300 profile shown by Edwards et al. (1987, 1989). There is some concern that these unresolved spikes are due to sky [O I] emission. However, the sky exposure used for subtraction was obtained immediately after the CW Tau integration and in the same part of the sky. In that spectrum the sky [O I] λ6300 line is about one-third the strength of the narrow feature in the raw CW Tau frame. The spikes in CW Tau are also shifted from the sky lines by about one resolution element (2.5 pixels).

The single [N II] peak at −115 km s^{-1} in CW Tau is consistent with the [N II] profile shown by Edwards et al. (1989). The weak (and noisy) [Fe II] lines appear to have profiles similar to [N II]. The double-peaked [S II] λ6716 and λ6731 profiles are markedly different from the broad asymmetric lines measured by Edwards et al. (1987) at higher resolution and from the λ4069 profile measured in 1988 February.

WL 22.—[Fe II] λ8617 is broad and blueshifted, with peaks at −180 and −360 km s^{-1} relative to the permitted lines. Other [Fe II] lines in the wavelength coverage are weaker and blended.

V 1331 Cyg.—The few forbidden lines within the wavelength coverage have blueshifted peaks and significant wings extending to near zero velocity. The small peak near [Fe II] λ8617 at +160 km s^{-1} is Fe I (401) 8621.6 Å, whose identification is confirmed by the presence of other members of this multiplet. [S II] λ4069 is severely blended with Fe I (43) λ4064, but its peak appears to be shifted by 40 km s^{-1} less than [Fe II].

RY Tau.—The [Fe II] is clearly more blueshifted than [O I] λ6300. The [S II] profile might be an artifact (§ 2).

TABLE 4

ADDITIONAL FORBIDDEN LINE STRENGTHS

Line ID	W_λ (Å)	Rel. Flux
—— V536 Aql (1988+1989)[1] ——		
[C I] (3F) 8727	0.06::	0.01::
[N II] (1F) 6583	3.35	0.33
[O I] (1F) 6300	10.3	1.00
[O II] (2F) 7319	0.90:	0.09:
[O II] (2F) 7330	0.90:	0.09:
[S II] (1F) 4069	15.5	1.57
[S II] (1F) 4076	4.20	0.42
[S II] (2F) 6716	1.68	0.17
[S II] (2F) 6731	3.11	0.31
[Fe II] (14F) 7155	0.48::	0.05::
[Fe II] (13F) 8617	0.33:	0.03:
[Ni II] (2F) 7378	<0.20	<0.02
—— CW Tau (1988+1990)[1] ——		
[N II] (1F) 6583	0.26	0.04
[O I] (3F) 5577	3.03	0.40
[O I] (1F) 6300	6.96	1.00
[S II] (1F) 4069	1.49	0.21
[S II] (2F) 6716	1.03:	0.14:
[S II] (2F) 6731	1.49	0.21
[Fe II] (14F) 7155	0.15::	0.02::
[Fe II] (14F) 7452	0.11::	0.01::
[Fe II] (13F) 8617	0.18::	0.02::
—— XZ Tau (1983) ——		
[N II] (1F) 6583	2.84	0.45
[O I] (1F) 6364	7.02	1.00
[S II] (2F) 6716	3.65	0.61
[S II] (2F) 6731	6.80	1.14
—— V380 Ori (1989) ——		
[O I] 6300 (1F)	0.25	1.00
[S II] (2F) 6731	<0.04	<0.14
[Ca II] (1F) 7291	0.23	0.71
[Fe II] (14F) 7155	0.20	0.64
[Fe II] (13F) 8617	<0.04	<0.09
[Ni II] (2F) 7378	<0.04	<0.12
—— R CrA (1989) ——		
[N II] (3F) 5755	<0.12	<0.08
[N II] (1F) 6583	0.14::	0.07::
[O I] (1F) 6300	2.01	1.00
[S II] (1F) 4069	0.15:	0.17:
[S II] (1F) 6716	0.22:	0.11:
[S II] (2F) 6731	0.41	0.20
[Fe II] (19F) 5262	0.06::	0.05::
[Fe II] (14F) 7155	0.43	0.22
[Fe II] (14F) 7388	0.23	0.12
[Fe II] (14F) 7452	0.15:	0.08:
[Ni II] (2F) 7378	0.20:	0.10:
—— HK Ori (1987) ——		
[Cr II] (1F) 8000	0.32	0.34
[Cr II] (1F) 8125	0.19	0.20
[Cr II] (1F) 8229	0.32::	0.34::
[Cr II] (1F) 8307	0.19:	0.20:
[Fe II] (14F) 7388	0.08::	0.11::
[Fe II] (14F) 7452	0.20	0.26
[Fe II] (13F) 8617	0.21	0.22
[Fe II] (13F) 8891	0.08	0.08
[Ni II] (2F) 7378	0.75	1.00
[Ni II] (2F) 7412	0.24	0.32
—— R Mon (1983+1987) ——		
[O I] (1F) 6364	pres.	—
[O II] (2F) 7319	<0.15	<0.07
[O II] (2F) 7330	<0.15	<0.07
[N II] (1F) 6583	0.44::	0.33::
[S II] (2F) 6716	0.82:	0.58:
[S II] (2F) 6731	1.43	1.00
[Ca II] (1F) 7291	0.08::	0.04::
[Cr II] (1F) 8000	0.31	0.09
[Cr II] (1F) 8125	0.21	0.06
[Cr II] (1F) 8229	0.07::	0.02::
[Cr II] (1F) 8307	0.19	0.05
[Fe II] (14F) 7388	0.24	0.11
[Fe II] (14F) 7452	0.29	0.13
[Fe II] (13F) 8617	0.94	0.25
[Fe II] (13F) 8891	0.34	0.09
[Ni II] (7F) 7308	0.04:	0.02:
[Ni II] (1F) 7378	1.22	0.57
[Ni II] (1F) 7412	0.52	0.24

[1] Only [S II] λ4069 and λ4076 were measured in 1988.

DF Tau.—The [O I] λ6300 and λ6364 profiles have two peaks at roughly −20 and −110 km s^{-1}, while [O I] λ5577 has just one peak at −20 km s^{-1}. The upper limit to the high-velocity flux in λ5577 in Table 2 accounts for the possible filling-in of a weak photospheric line at −50 km s^{-1}. (The intrinsic strength of the photospheric line was estimated from other nearby absorptions assuming the absorption ratios are like those in weak line TTSs with no forbidden emission.) The λ6300 profile has a relatively weaker low-velocity peak than was reported by Edwards et al. (1987), measured 1984 December, and Hartmann & Raymond (1989), measured 1988 January. The differences appear too large to be caused by the 50% lower spectral resolution of the present data. The blueshifted [N II] λ6583 line measured by Edwards et al. (1989) is not detected here.

DG Tau.—The [O I], [S II] and [Fe II] lines measured 1990 February have strong peaks at −40 to −50 km s^{-1}, while the [N II] peaks at −230 km s^{-1} with almost no emission to the red of −100 km s^{-1}. Significant emission appears in [O I] λ6300 between −430 km s^{-1} and +40 km s^{-1}. The profiles clearly varied between 1987 December, 1990 February, and the various measurements reported in the literature. In particular, the [Ca II] and [Fe II] lines had relatively more high-velocity (blueshifted) emission in 1987 December than in 1990 February. The [Ca II] profiles changed most dramatically, from sharp single peaks centered at −215 km s^{-1} in 1987 to broader twin peaks at roughly −230 and −60 km s^{-1} in 1990. Unfortunately, [O I], [S II], and [N II] were measured only in 1990 February, but there are published profiles of these lines in Hartmann & Raymond (1989), Edwards et al. (1989), and Appenzeller et al. (1984). In the earliest of these measurements (Appenzeller et al. 1984—observed 1983 December) the [O I] 6300 Å line has two distinct peaks at −162 and −40 km s^{-1} (in the rest frame of the star) with a ratio of blue to red peak heights of ∼0.8. In the Hartmann & Raymond (1989) data (measured 1988 January) a high-velocity peak is clearly present at about −230 km s^{-1} (in the stellar frame) with a relative strength of blue to red of ∼0.55. In 1990 February (Fig. 1*o*) the high-velocity component no longer constitutes a separate peak, and at −230 km s^{-1} the line has only ∼0.25 of the (low-velocity) peak flux. Note that the spectral resolution is the same here as in Appenzeller et al. but ∼35% lower than in Hartmann & Raymond (19 km s^{-1} vs. 12 km s^{-1}). If there is a profile difference due to the resolution it would be in the sense of not resolving the peak near zero in Figure 1*o*, which would only strengthen the case for a weakening high-velocity peak. The [S II] profiles published by Appenzeller et al. (1984) are too noisy for meaningful comparisons. The [N II] and [O I]

TABLE 5

KK OPH FORBIDDEN LINES[a]

Line ID	W_λ (Å)	Rel. Flux	Line ID	W_λ (Å)	Rel. Flux
[C I] (3F) 8727	0.18	0.07	[Fe II] (20F) 4874	0.19:	0.19:
[N I] (1F) 5200	<0.10	<0.08	[Fe II] (20F) 4890	0.35	0.34
[N II] (3F) 5755	<0.05	<0.03	[Fe II] (20F) 4905	0.32	0.31
[N II] (1F) 6583	0.35	0.19	[Fe II] (20F 4947)	0.08:	0.08:
[O I] (3F) 5577	<0.05	<0.04	[Fe II] (20F) 4951	0.16	0.15
[O I] (1F) 6300	1.75	1.00	[Fe II] (20F) 4973	0.18	0.17
[O I] (1F) 6364	0.58	0.32	[Fe II] (20F) 5006	0.26	0.24
[O II] (2F) 7319	0.44:	0.21:	[Fe II] (20F) 5043	0.04::	0.04::
[O II] (2F) 7330	0.40:	0.19:	[Fe II] (18F) 5108	0.15	0.13
[S II] (1F) 4069	0.21	0.20	[Fe II] (19F) 5112	0.29	0.26
[S II] (2F) 6716	0.10:	0.05:	[Fe II] (18F) 5158	1.18	1.02
[S II] (2F) 6731	0.19	0.10	[Fe II] (19F) 5159	blend	—
[Ca II] (1F) 7291	0.15::	0.07::	[Fe II] (35F)? 5164	0.17	0.15
[Ca II] (1F) 7324	present	—	[Fe II] (18F) 5182	0.08::	0.07::
[Cr II] (1F) 8000	0.37	0.15	[Fe II] (19F) 5220	0.25	0.21
[Cr II] (1F) 8125	0.29	0.12	[Fe II] (19F) 5262	0.67	0.55
[Cr II] (1F) 8308	0.19:	0.08:	[Fe II] (18F) 5269	0.13:	0.11:
[Fe II] (23F) 4114	0.04:	0.04:	[Fe II] (18F) 5273	0.40	0.33
[Fe II] (21F) 4177	0.09	0.09	[Fe II] (19F) 5297	0.12:	0.10:
[Fe II] (21F) 4244	0.77	0.83	[Fe II] (19F) 5334	0.60	0.48
[Fe II] (21F) 4277	0.52	0.57	[Fe II] (19F) 5376	0.39	0.30
[Fe II] (7F) 4287	0.42	0.46	[Fe II] (17F) 5413	0.08::	0.06::
[Fe II] (21F) 4306	0.16	0.18	[Fe II] (18F) 5433	0.07::	0.05::
[Fe II] (21F) 4320	0.27	0.30	[Fe II] (17F) 5496	0.11::	0.08::
[Fe II] (21F) 4347	0.11:	0.12:	[Fe II] (17F) 5527	0.21	0.15
[Fe II] (21F) 4353	0.06:	0.07:	[Fe II] (17F) 5746	0.19:	0.13:
[Fe II] (21F) 4358	0.71	0.81	[Fe II] (34F) 5747	blend	—
[Fe II] (7F) 4359	blend	—	[Fe II] (31F) 6809	0.06::	0.03::
[Fe II] (21F) 4372	0.15	0.17	[Fe II] (31F) 6966	0.10:	0.05:
[Fe II] (6F) 4383	0.08::	0.09::	[Fe II] (14F) 7155	0.65	0.32
[Fe II] (7F) 4414	0.28	0.33	[Fe II] (14F) 7172	0.30	0.15
[Fe II] (6F) 4416	0.62	0.72	[Fe II] (14F) 7388	0.13	0.06
[Fe II] (7F) 4452	0.14	0.16	[Fe II] (14F) 7452	0.23:	0.11:
[Fe II] (6F) 4458	0.31	0.35	[Fe II] (13F) 8617	0.35	0.14
[Fe II] (4F) 4640	0.16	0.17	[Ni II] (4F) 3993	0.10:	0.09:
[Fe II] (4F) 4664	0.04::	0.04::	[Ni II] (3F) 4326	0.05:	0.06:
[Fe II] (4F) 4728	0.25	0.26	[Ni II] (2F) 6667	0.18:	0.10:
[Fe II] (20F 4775)	0.20:	0.20:	[Ni II] (8F) 6814	0.04::	0.02::
[Fe II] (20F) 4815	0.64	0.64	[Ni II] (7F) 7256	0.11::	0.05::
			[Ni II] (7F) 7308	0.08::	0.04::
			[Ni II] (2F) 7378	0.95	0.44
			[Ni II] (2F) 7412	0.37	0.17

NOTE.—Measurements are from 1989 April.

λ5577 lines shown by Edwards et al. (1989), whose measurement dates are not given, do not appear significantly different from the profiles measured here in February 1990.

The [O II] lines of DG Tau appear exclusively blueshifted, with velocities comparable to the high velocity [Ca II] and [N II] peaks. The [O II] identifications are not definitive because their centroids do not quite match in velocity (Fig. 1*o*). However, using average wavelengths for plotting these close doublets (§ 3.2) might account for the shift of ~33 km s^{-1} between the two peaks in Figure 1. The centroids in the stellar rest frame are at 7313.3 and 7323.5 Å in the 1987 December spectrum. Their identification with [O II] is supported by the following: (1) the velocities of the blueshifted peaks approximately match the [Ca II] and [N II] lines; (2) the ionization/excitation required for [O II] is consistent with the presence of strong [N II] (see § 4.3.3 below); (3) the relative strength of the two measured features is consistent with the [O II] oscillator strengths; (4) the broadening of the two features between 1987 and 1990 is consistent with the broadening of [Ca II] and other forbidden lines (Figs. 1*o* and 1*p*) but inconsistent with the nearly constant widths of the permitted lines (PP1); and (5) there are no better alternative identifications. There may be some contribution to the blue wings of the 7313.3 and 7323.5 Å features from Fe II (73) 7308.0, 7310.2, and 7320.7 Å (corresponding to −460, −370, and +60 km s^{-1} relative to [O II] 7319.2 in Fig. 1). Other lines of Fe II (73) are observed (e.g., at 7462 and 7712 Å). However, the Fe II lines are shifted by $\gtrsim$115 km s^{-1} from the centroids—and by $\gtrsim$150 km s^{-1} from the peaks—of the measured [O II] features. Therefore Fe II cannot account for the observed peaks and cannot contribute more than ~20% to the total flux.

The sky spectrum used to subtract the telluric [O I] lines was

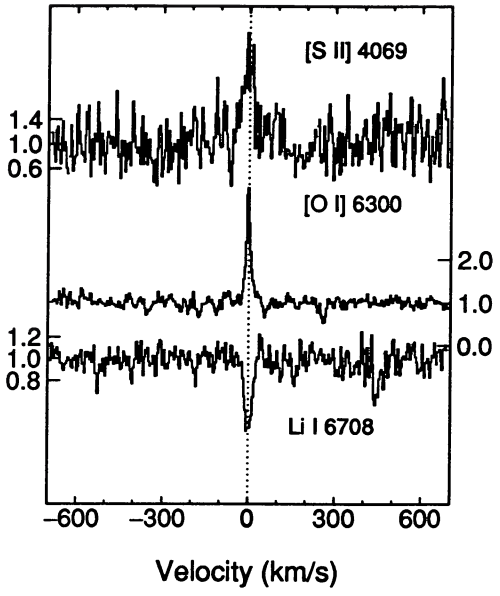

FIG. 1*a*—HM 32

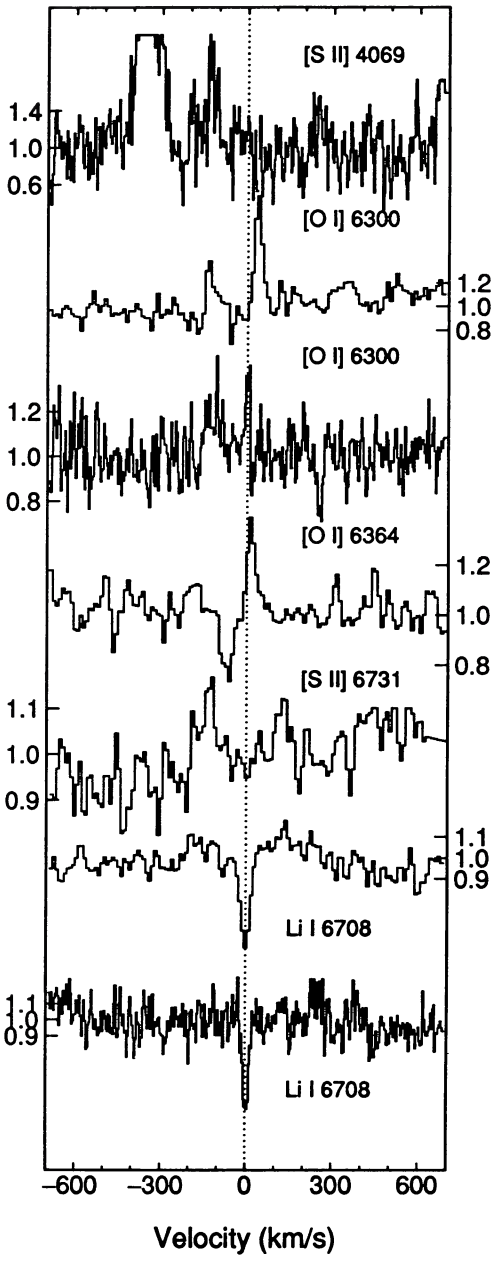

FIG. 1*b*—HM Lup

FIG. 1.—(*a*) HM 32: 1989 April. Line profiles from the short-wavelength echelle data are plotted on a velocity scale in the stellar rest frame. The stellar velocity was measured from the Li I line (Table 1). Tick marks next to each profile indicate the intensity relative to the continuum. (*b*) HM Lup: 1989 April. The Li I absorption and [O I] λ6300 emission lines are plotted from both 1989 April spectra, with the blue echelle measurements nearer the bottom. In this and subsequent plots the tops of strong emission lines unrelated to the unidentified feature are sometimes truncated. The truncated emission at −370 km s^{-1} in the [S II] λ4069 plot is Fe I (43) 4063.6 Å. (*c*) RU Lup: 1989 April. The truncated emission to the left of [N II] λ6583 plot is the red wing of Hα. (*d*) AS 205: 1989 April. (*e*) S CrA: 1989 April. (*f*) VV CrA: 1989 April. (*g*) VV CrA: 1990 April. The velocities are in the stellar rest frame measured in 1990. [Ca II] λ7324 and the two [O II] lines are blended with each other and with several Fe II lines. (*h*) AS 353A: 1989 April. The lines of [O I] and possibly [S II] and [Fe II] have multiple blue and redshifted peaks. The lower [Fe II] λ8617 profile is from 1987 June. (*i*) V536 Aql. [Fe II] λ8617 and [S II] λ4069 were measured 1988 September. All others are from 1989 April. [Ca II] λ7324 and the two [O II] lines are blended. (*j*) CW Tau. [S II] λ4069 was measured 1988 September. All others are from 1990 October. (*k*) WL 22: 1988 September. The velocities are heliocentric. (*l*) V1331 Cyg: 1988 September. The velocities are heliocentric. (*m*) RY Tau: 1990 October. (*n*) DF Tau: 1990 October. (*o*) DG Tau: 1990 February. [Ca II] λ7324 and the two [O II] lines are blended. Some of the unresolved central spike in [O I] λ5577 might be residual sky emission after incomplete subtraction. (The sky and source spectra were obtained almost 2 hr apart.) (*p*) DG Tau: 1987 December. The velocities are in the stellar rest frame measured in 1990. [Ca II] λ7324 and the two [O II] lines are blended. (*q*) HL Tau. The [N II] and [S II] were measured in 1983 December. All others are from 1987 December. The velocities are heliocentric. (*r*) XZ Tau: 1983 December. The velocities are heliocentric. (*s*) RW Aur: 1990 February. The profiles sometimes have redshifted and blueshifted peaks. (*t*) RW Aur: 1987 December. The velocities are in the stellar rest frame measured in 1990. The [Fe II] line may have multiple blueshifted and redshifted peaks. (*u*) DK Tau: 1990 October.

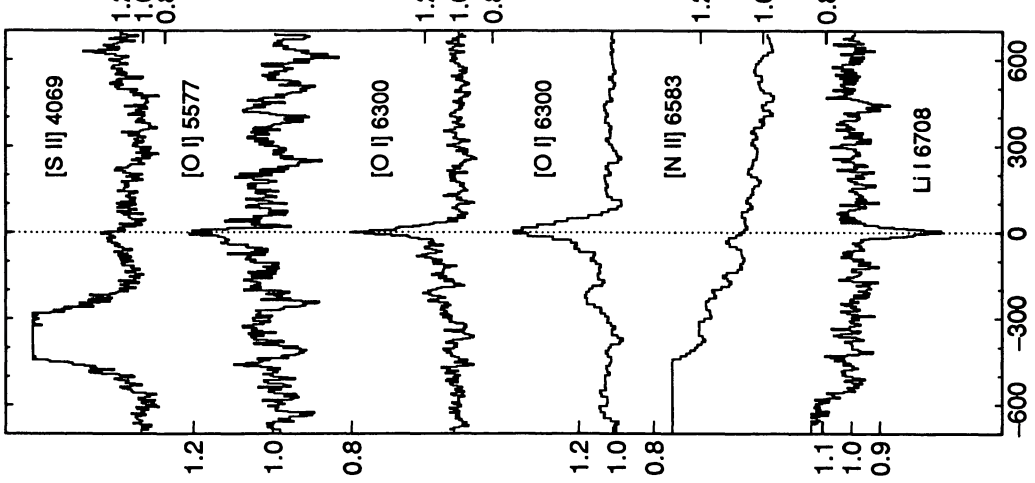

FIG. 1*d*—AS 205

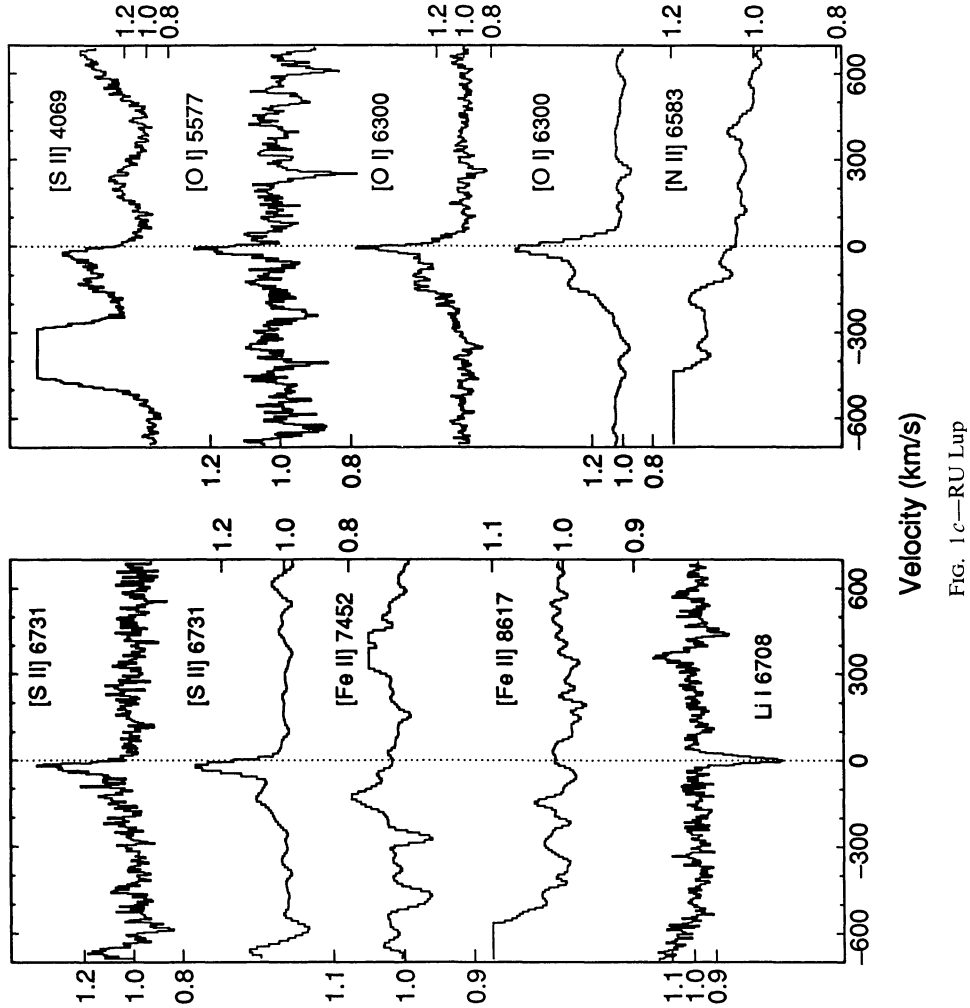

FIG. 1*c*—RU Lup

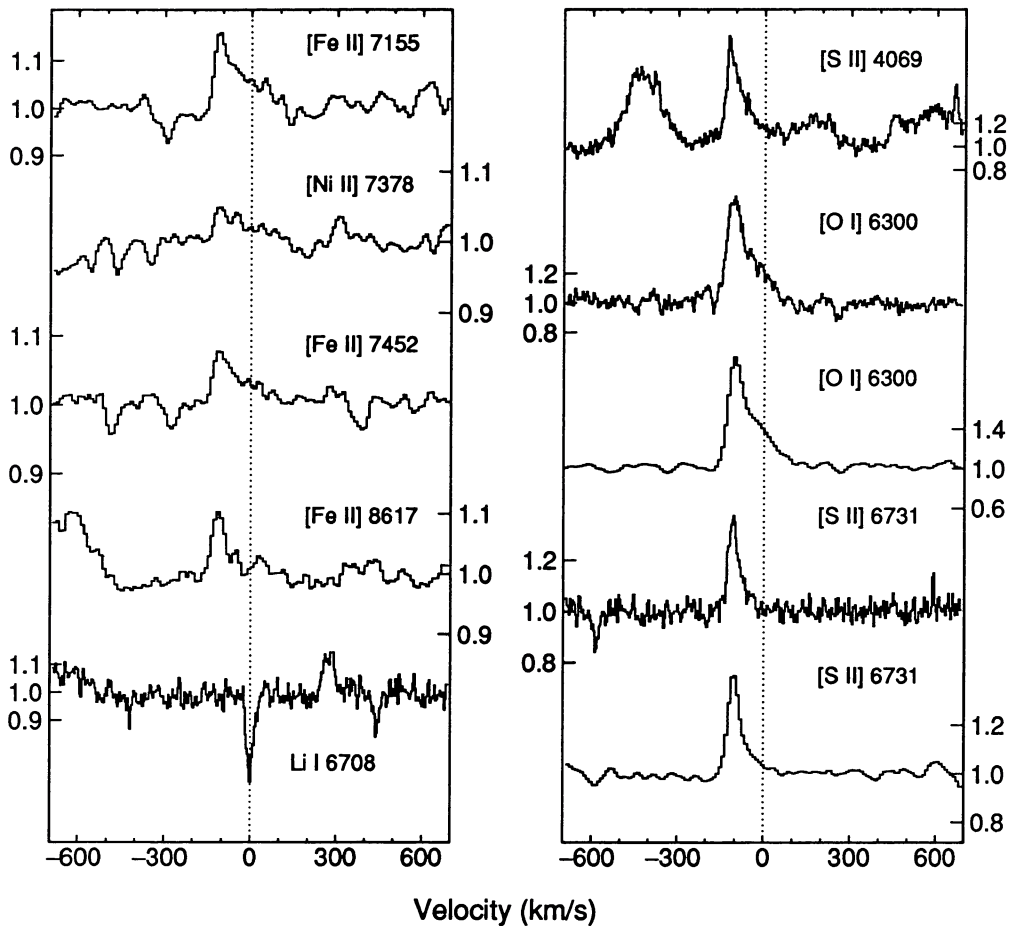

FIG. 1*e*—S CrA

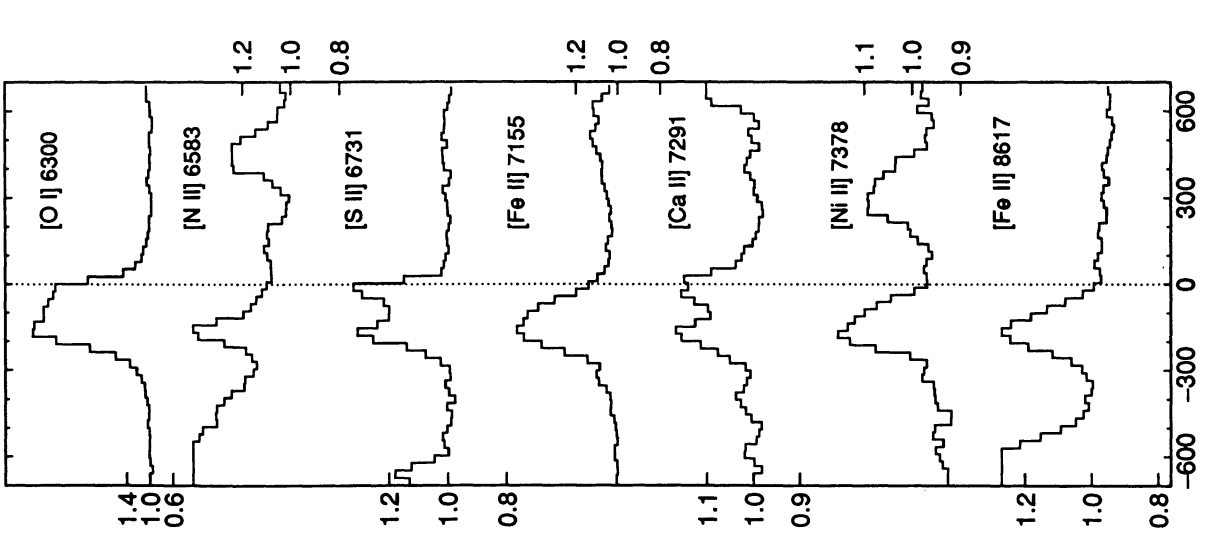

FIG. 1*g*—VV CrA (1990 Apr)

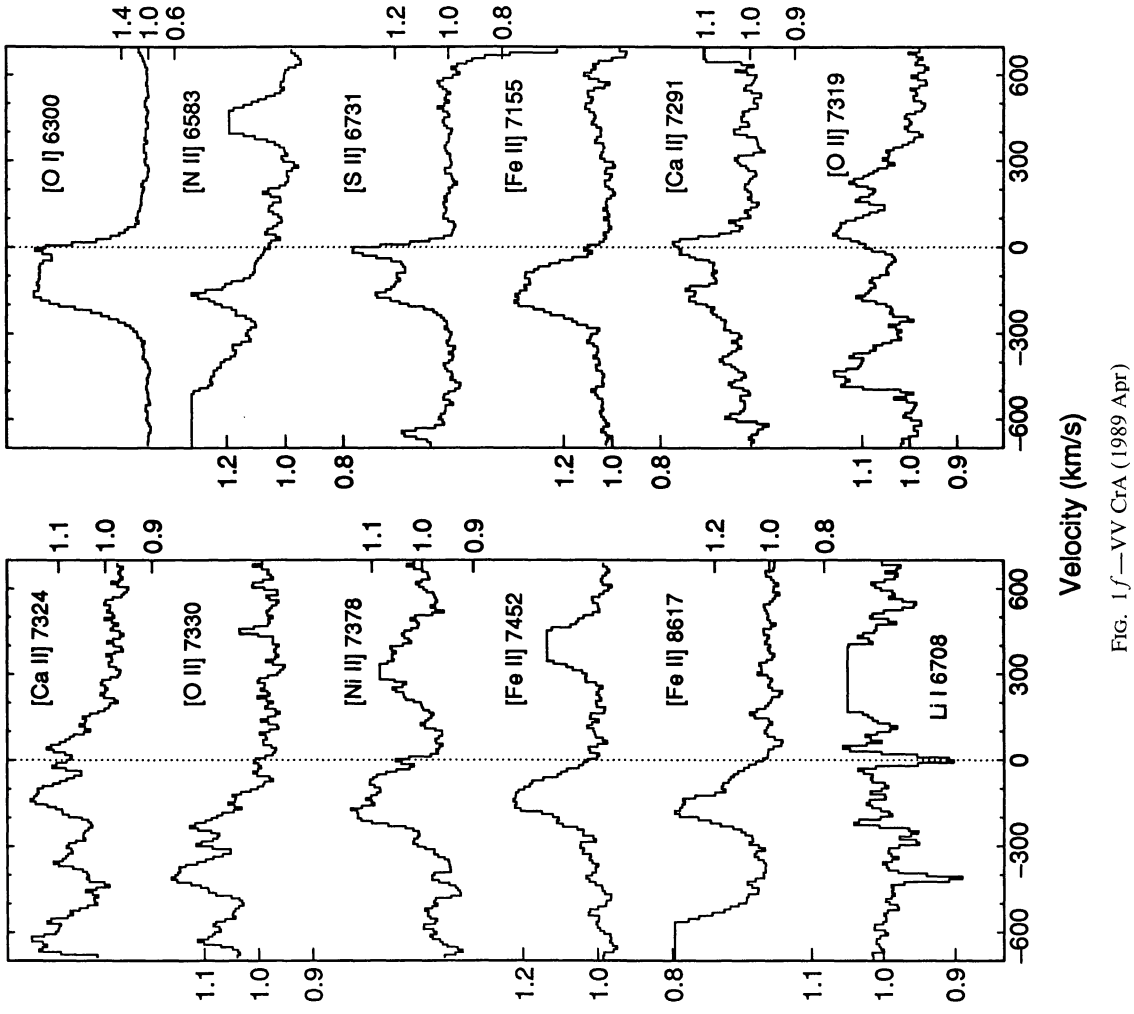

FIG. 1*f*—VV CrA (1989 Apr)

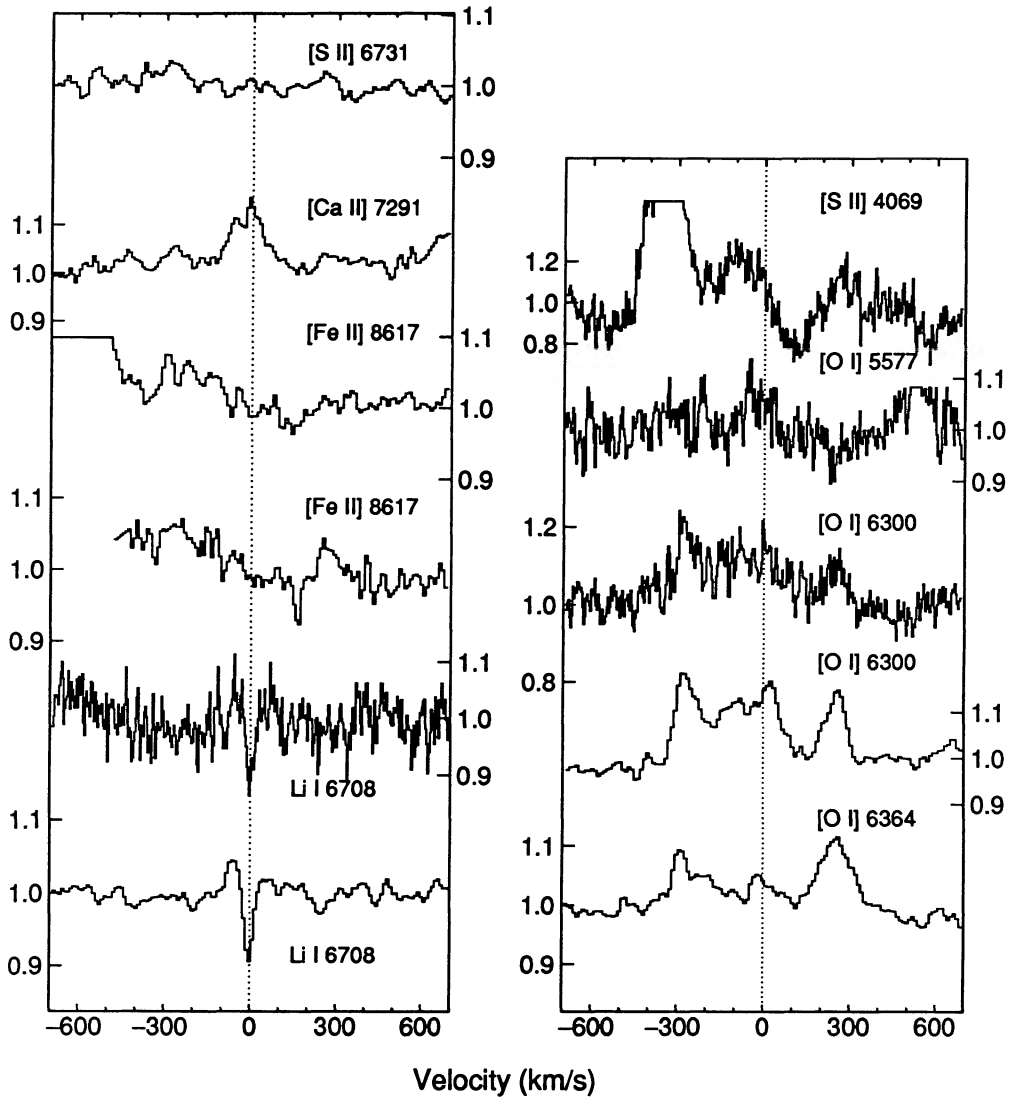

FIG. 1*h*—AS 353A

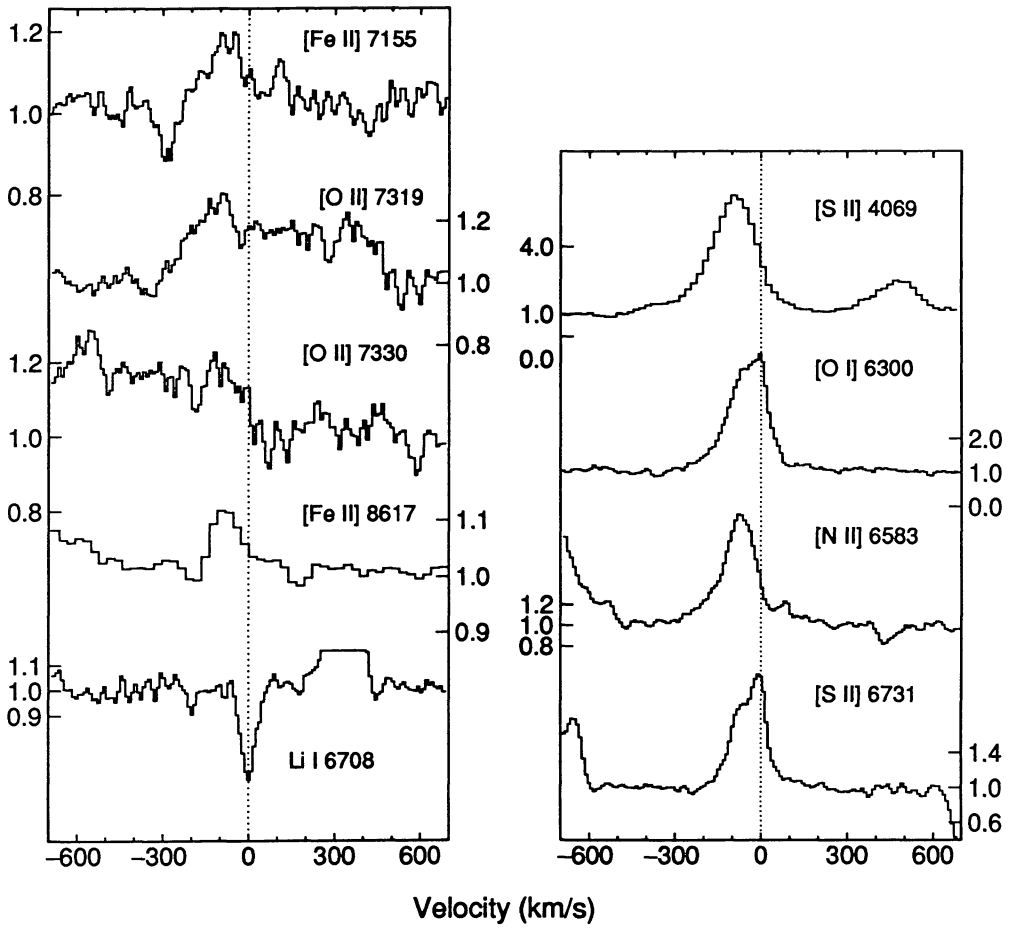

FIG. 1*i*—V536 Aql

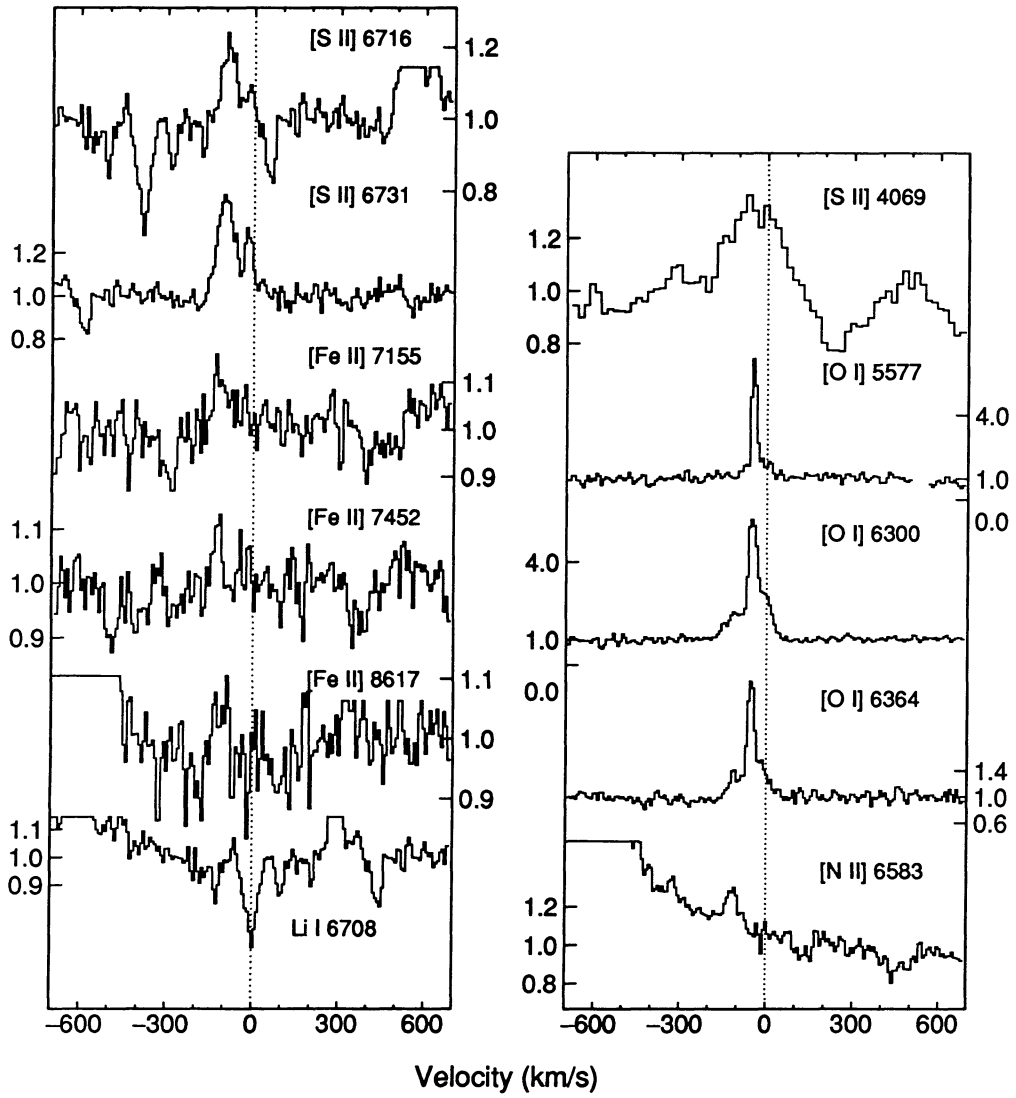

FIG. 1*j*—CW Tau

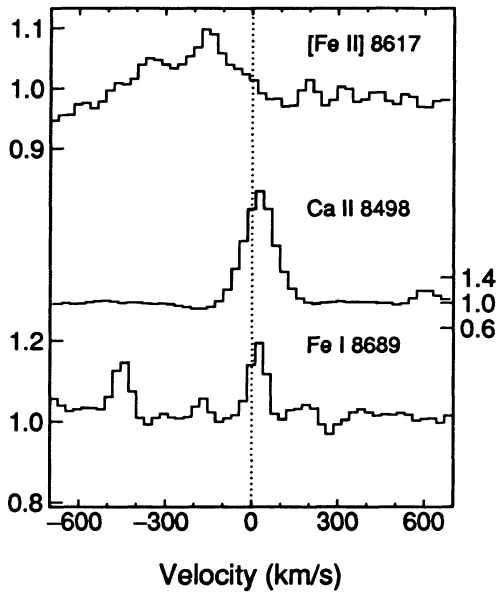

FIG. 1*k*—WL 22

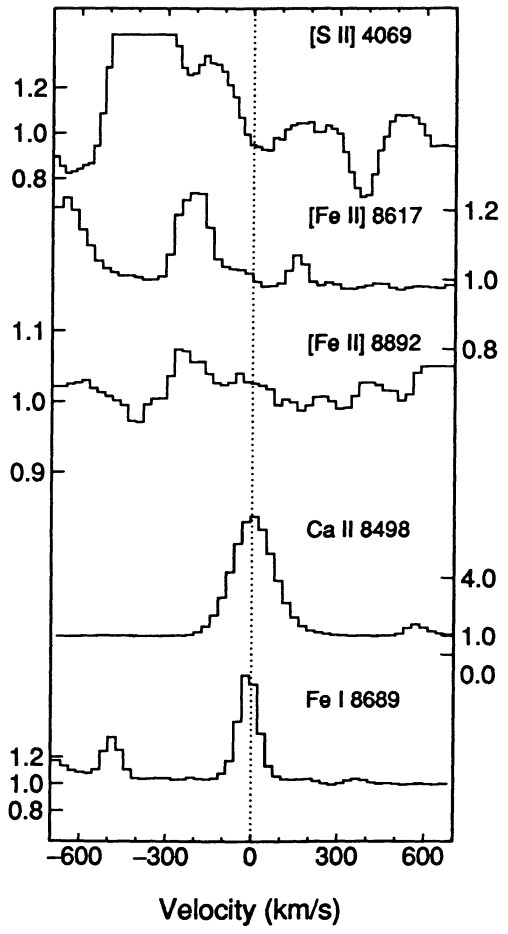

FIG. 1*l*—V1331 Cyg

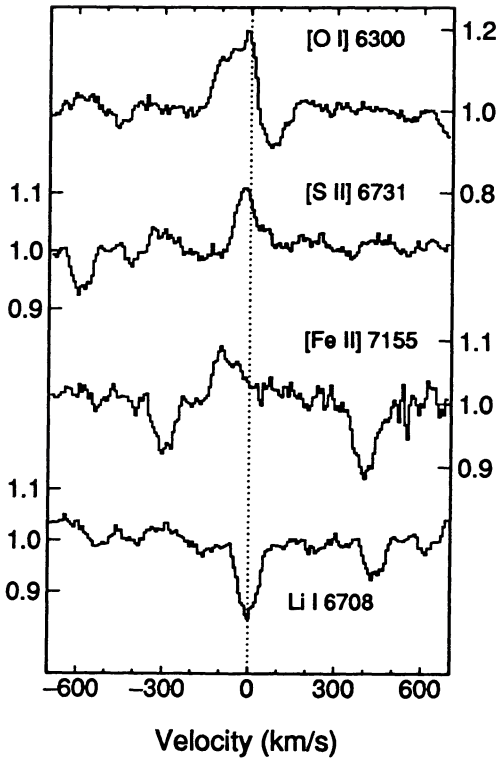

FIG. 1*m*—RY Tau

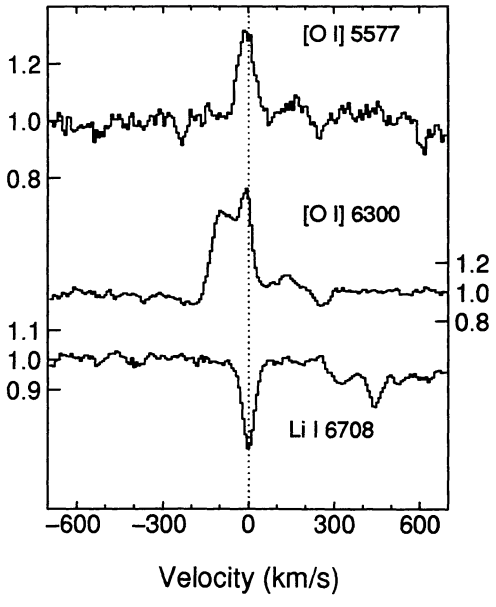

FIG. 1*n*—DF Tau

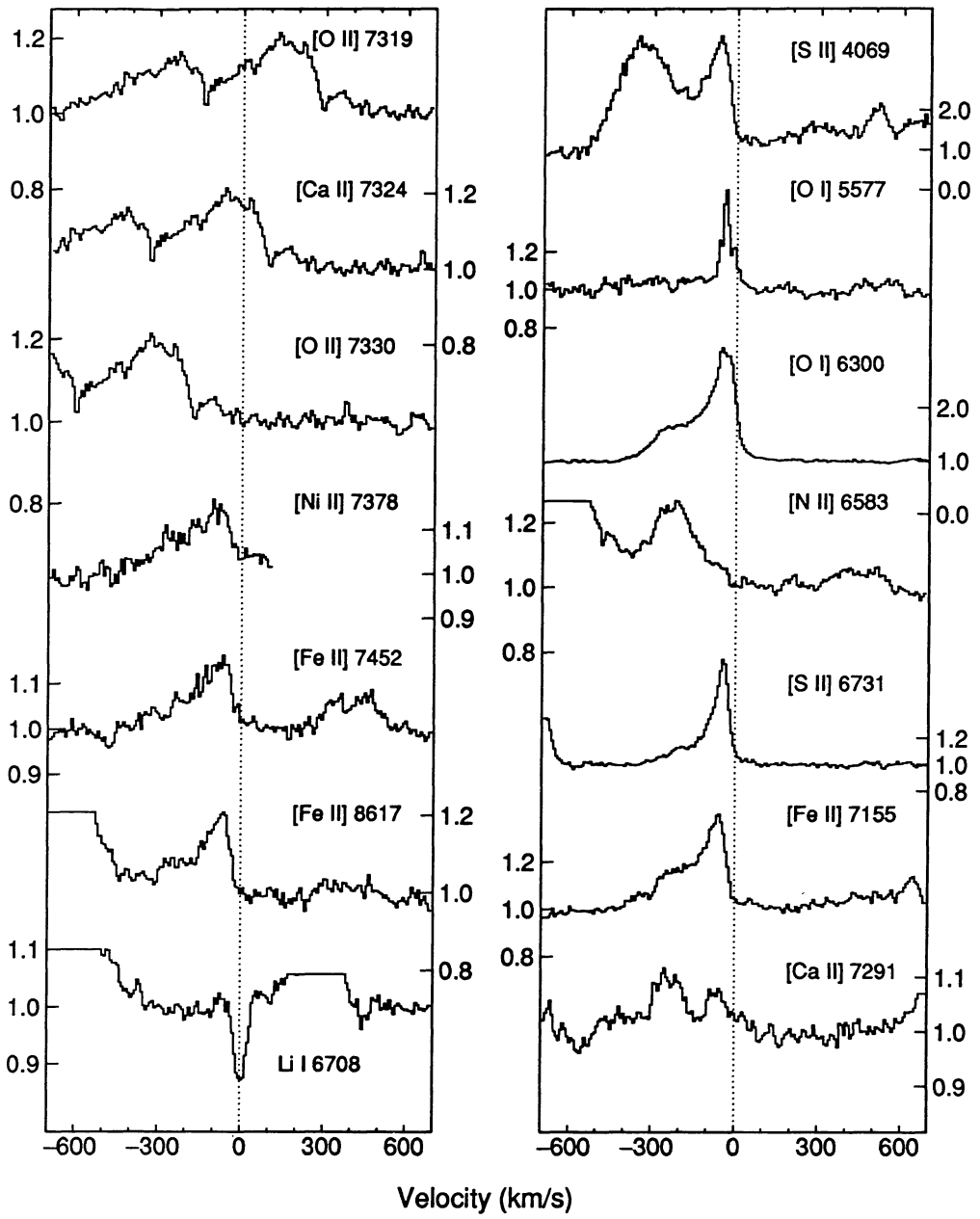

FIG. 1*o*—DG Tau (1990 Feb)

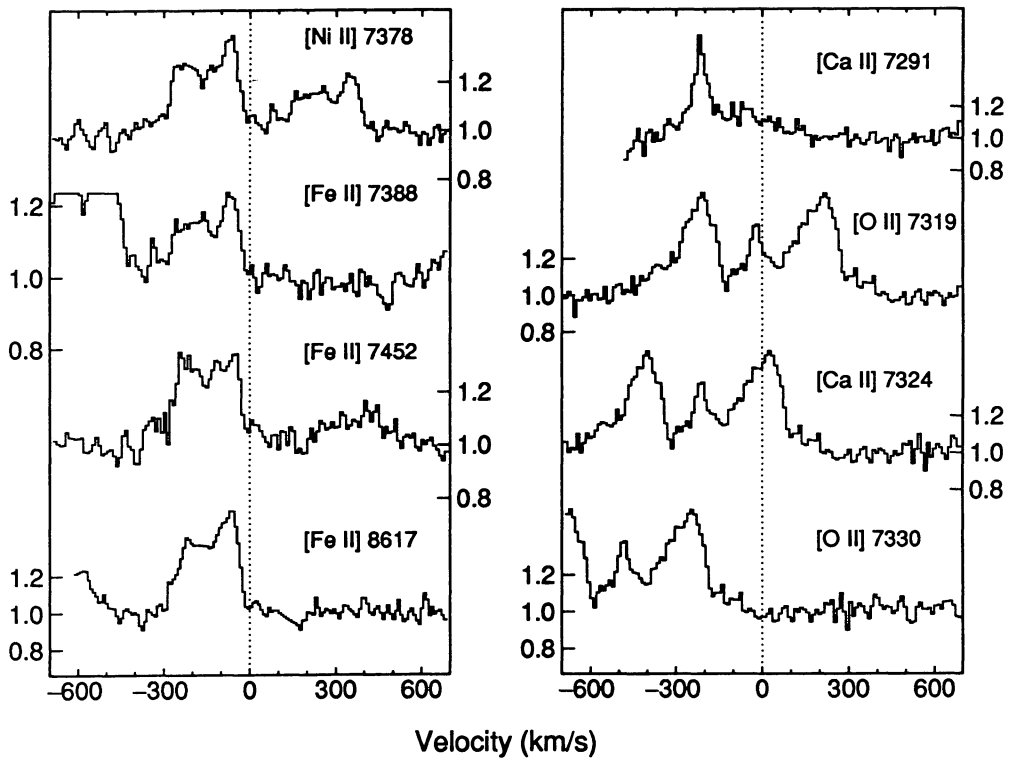

FIG. 1*p*—DG Tau (1987 Dec)

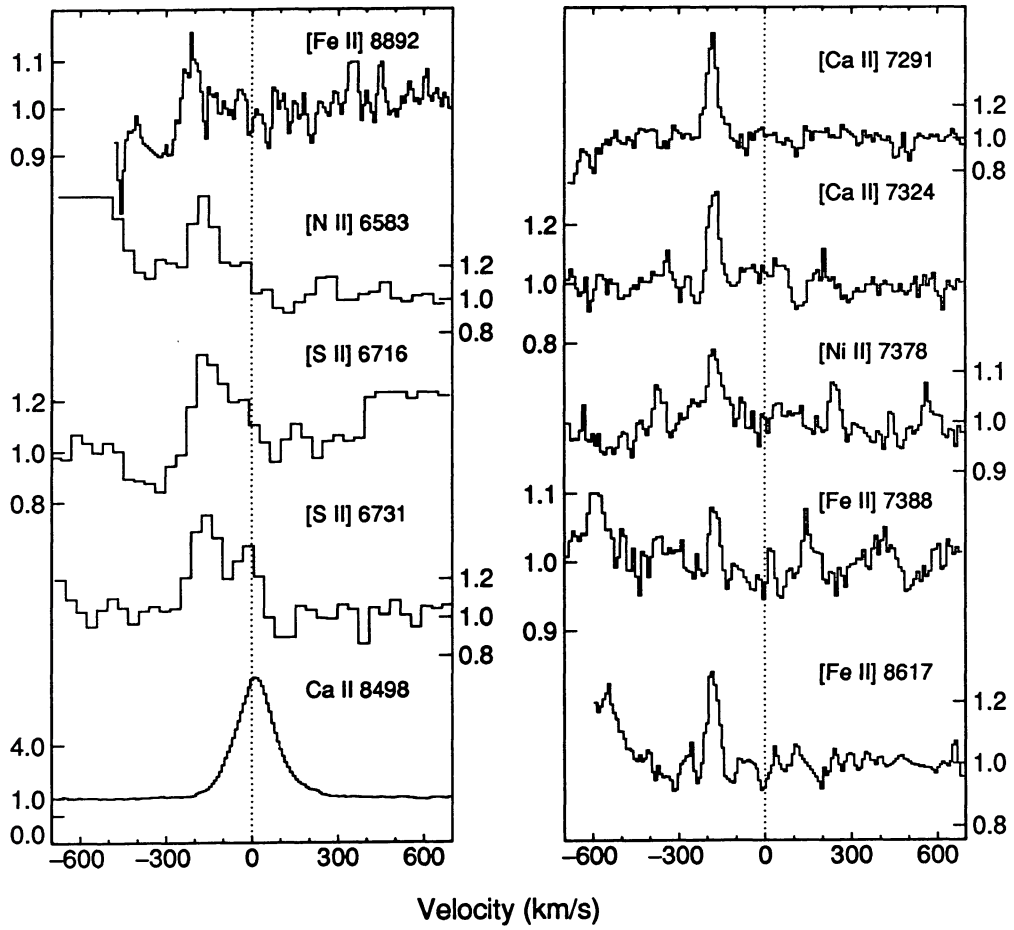

FIG. 1*q*—HL Tau

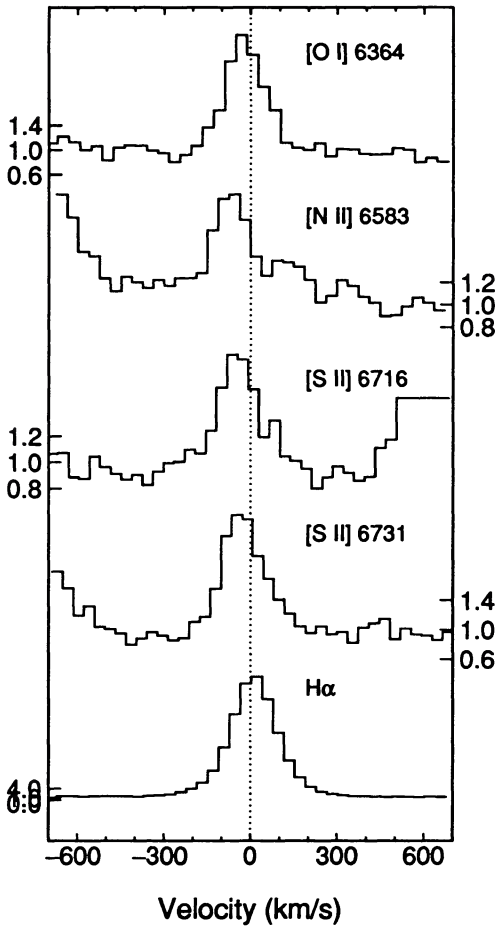

FIG. 1*r*—XZ Tau

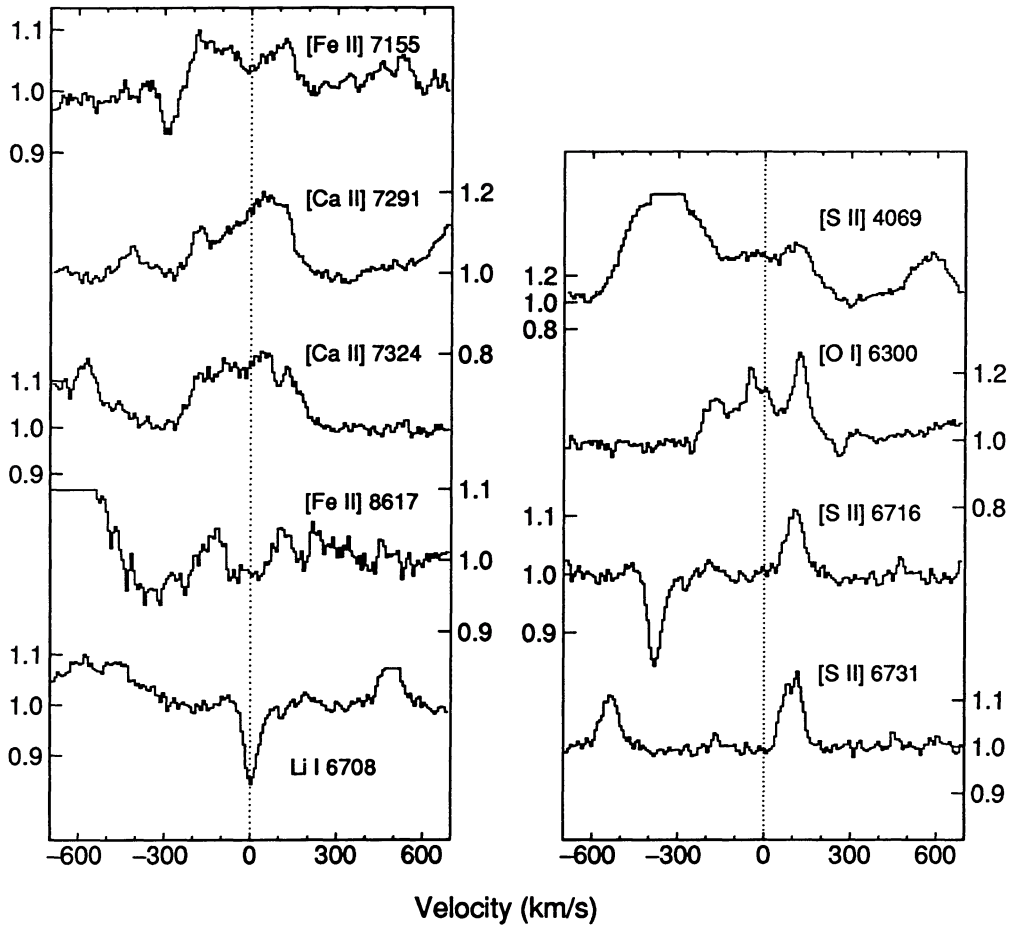

FIG. 1*s*—RW Aur (1990 Feb)

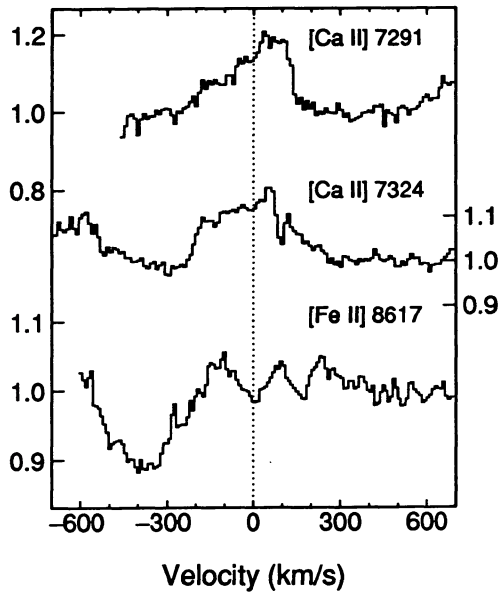

FIG. 1*t*—RW Aur (1987 Dec)

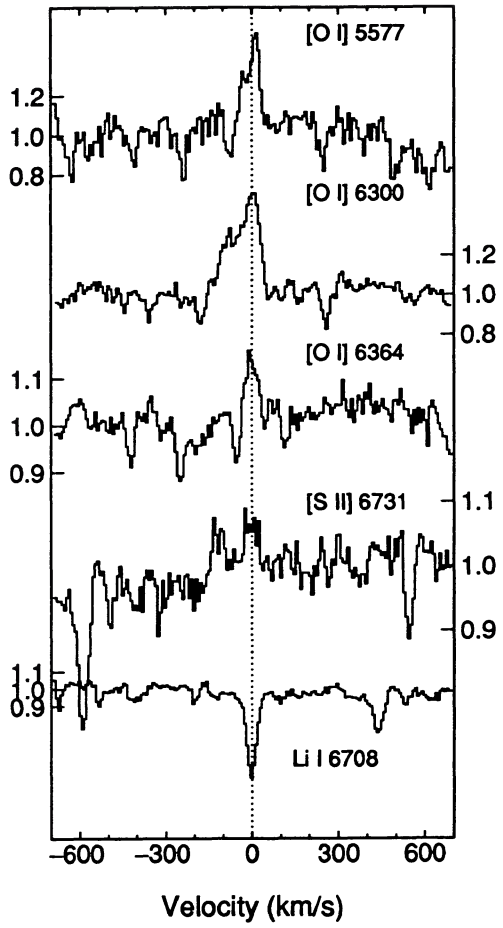

FIG. 1*u*—DK Tau

obtained ~1 hr before the 1990 DG Tau exposure. Subtracting this spectrum reduced λ5577 by ~25% and reduced the low-velocity peaks in λ6300 and λ6364 by only ~10%. Multiple sky exposures throughout the night showed that variability in the sky emission might cause errors up to a factor of ~2 in the sky contributions. Finally, there may be weak [Fe II] lines at short wavelengths, such as λ4358, λ4815, λ5262, and λ5334. Their identifications could not be confirmed because of blends.

HL Tau.—The lines measured at high resolution, [Ca II], [Fe II], and [Ni II] in December 1987, have single peaks at about −200 km s^{-1} relative to the permitted Ca II. The FWHM are typically ~50 km s^{-1}, although the peaks may be unresolved. The [N II] line (measured at lower resolution in 1983) is unresolved and blueshifted to velocities similar to [Ca II], [Fe II], [Ni II], while the [S II] profiles (also 1983) are broad, with significant emission near the rest velocity. There appears to be a velocity shift between the [Ca II], [Fe II], and [Ni II], lines measured in 1987 and the [S II] and [N II] profiles measured in 1983. The [S II] and [N II] measurements are consistent with the higher resolution profiles shown by Edwards et al. (1989), Solf (1989), and Mundt et al. (1990).

XZ Tau.—The forbidden lines are blueshifted by ≳40 km s^{-1} compared to the symmetric Hα profile. The largest shift appears in [N II] λ6583 at about −80 km s^{-1}. The [O I] and [S II] profiles are consistent with previous measurements by Appenzeller et al. (1984) and Solf (1989).

RW Aur.—This source has complex forbidden profiles with both red- and blueshifted components. The [O I] λ6300 line has three distinct peaks, at roughly −180, −40, and +115 km s^{-1} in the stellar rest frame. It is possible that λ6300 is blended with some Fe I emission because Fe I is generally strong in RW Aur. The most likely contributors are Fe I (62) 6297.8 Å (at −116 km s^{-1}) and Fe I (816) 6301.5 and 6302.5 Å (at +60 and +108 km s^{-1}, respectively). The Fe I contribution cannot be judged precisely from other lines in the same multiplets because those lines, if present, are also blended with other features. However, upper limits on Fe I (816) λ6400 and λ6412 and Fe I (62) λ6431 suggest that the emission from Fe I near ~6300 Å contributes <10% of the flux in each of the velocity intervals in Table 3 (assuming relative line strengths as in Moore 1972). [O I] λ6364 (not shown) is badly blended with emission from Fe II (40) 6369.4 Å, Fe I (13) 6353.8 and 6358.7 Å, and broad P Cygni–shaped lines of Si II (2) 6347.1 and 6371.4 Å (see notes on AS 353A for relative velocities).

The [S II] λ6716 and λ6731 lines of RW Aur are *only redshifted,* with peak velocities at +100 km s^{-1}. [S II] λ4069 has emission at similar redshifts, but also has considerable flux near zero and at blueshifted velocities. The blue wing of λ4069 blends with Fe I (43) λ4064. There may be some contribution to the red wing of λ4069 from Fe I (43) 4071.7 Å at +222 km s^{-1}. However, this Fe I line should have ≲30% of the peak intensity of λ4069 (based on the strength of other lines in this multiplet; see also Herbig 1945 and Moore 1972). The [S II] λ4076 line is badly blended with Sr II (1) 4077.7 Å (also Joy 1945).

[Ca II] λ7291 has broad emission between roughly −250 and +180 km s^{-1}, with a well-defined peak in the blue wing at −200 km s^{-1}. The blueshifted peak might be an artifact of the imperfect removal of telluric absorption lines. The [Ca II] λ7291 profile should have some contribution from Fe II (72) 7289.1 Å (at −100 km s^{-1}), but this cannot account for the peak at −200 km s^{-1}. The peak at −415 km s^{-1} is due to He I (45) 7281.3 Å. The two most reliable [Fe II] measurements, λ7155 and λ8617, appear to have both red- and blueshifted peaks. The main features of the λ8617 profile are confirmed by their presence in both the 1990 and 1987 spectra (λ7155 was not measured in 1987). Unlike V1331 Cyg (above) there is no evidence for Fe I on the red side of λ8617. The dip toward the blue of λ8617 in the 1987 spectrum is an artifact of the continuum normalization. [Fe II] λ7454, if present, is overwhelmed by strong emission from Fe II (73) 7449.3 Å.

DK Tau.—The [O I] λ6300 line is broad with a strong blueshifted component, while λ5577 is narrower and centered at roughly the stellar rest velocity. The upper limit on the high-velocity flux in λ5577 in Table 2 accounts for the possible filling-in of the weak photospheric line at −50 km s^{-1} (see notes on DF Tau). The double-peaked [S II] λ6731 profile is unlike any of the spurious features recorded at this wavelength in the October 1990 spectra (§ 2). This detection therefore appears secure. The [S II] λ6716 line may be present, but it is badly contaminated by photospheric absorptions, e.g., Ca I (32) 6717.7 Å.

V380 Ori.—The forbidden lines are resolved with FWHM between ~110 and ~150 km s^{-1}. There were no significant

changes between the 1989 April and 1990 February measurements. The centroids of the [O I] and [Fe II] lines appear slightly ($\lesssim$20 km s^{-1}) blueshifted with respect to Pa 12 and the Ca II triplet. The forbidden lines are clearly blueshifted by $\sim$25 km s^{-1} relative to the Hα centroid measured in 1990.

Z CMa.—The [O I] λ6300 and λ6364 lines are present but badly contaminated by photospheric absorptions. [Ca II] λ7291 is the strongest well-measured line.

KK Oph.—The forbidden lines are slightly blueshifted from the stellar rest velocity given by Finkenzeller (1985). The widths of the strong [O I], [Fe II], and [Ni II] lines are typically FWHM $\sim$ 50–80 km s^{-1}. The broad wings in [O I] λ6300 are less prominent here than in Finkenzeller (1985). The [N II] has FWHM $\sim$ 170 km s^{-1} with no narrow core and a strong blue asymmetry. The [S II] widths are intermediate between [O I] and [N II]. [O II] λ7319 and λ7330 are present as part of a blend with [Ca II] λ7324. Unlike VV CrA and DG Tau discussed above, the Fe II (73) lines should not contribute at all to the blend because Fe II is very weak. The blended [O II] profiles appear at least as broad as the [N II].

R CrA.—The forbidden lines have strong blueshifted wings. A few of the strongest lines in the visible [Fe II] multiplets (e.g., 18 and 19) are marginally detected but not shown in the figure.

PV Cep.—The [Fe II] λ8617 line has a strong peak at $-$280 km s^{-1} and significant emission between $-$420 and $\sim$0 km s^{-1} relative to the permitted line velocities. Other members of the [Fe II] (13F) multiplet are detected, such as λ8892, but their profiles are contaminated by poorly subtracted sky lines (PP2).

LkHα 233.—The unresolved [Fe II] lines are blueshifted by $\sim$150 km s^{-1} compared to the peaks of the permitted Ca II lines.

R Mon.—The forbidden lines have strong blueshifted wings as well as peaks that are blueshifted 20–30 km s^{-1} compared to the permitted lines. The [Ca II] detections are uncertain because the lines are weak and do not match in velocity. [N II] λ6583 is marginally detected.

4. DISCUSSION

4.1. *Line Profile Variability*

The existing data are too sparse to draw conclusions on the nature or frequency of the profile variations. The most dramatic and conclusive profile changes occurred in DG Tau (§ 3.3). The large differences between the 1987 and 1990 data could be part of a gradual trend occurring in the profiles (e.g., [O I]) since at least 1983. There is also evidence for variability in CW Tau, DF Tau, KK Oph, and perhaps AS 353A, based on comparisons with the literature.

4.2. *Kinematics and Morphology*

4.2.1. *Line Velocity Components*

The ensemble forbidden profiles can be divided into four components: (1) narrow rest-velocity lines, (2) low-velocity line peaks or wings, (3) high-velocity blueshifted peaks or wings, and (4) high-velocity redshifted peaks. The velocities and relative strengths of these components can differ from object to object, but their common appearance provides a basis for a general discussion of the line profiles. The physical relationship between the components is unspecified, but the fact that they represent gas at different line-of-sight velocities, and appear with different relative strengths in different objects and with different relative strengths in different lines of the same object, implies that the emitting regions are not cospatial and are possibly unrelated. Thus the four line components might represent four distinct emitting environments that are generic to pre–main-sequence stars.

The rest-velocity lines are generally narrow, symmetric, and single-peaked, with FWHM ranging from $\lesssim$15 km s^{-1} in HM 32 to >50 km s^{-1} in some of the Herbig Ae–Be stars. Among TTSs, these lines appear almost exclusively in sources with weak and narrow permitted metal lines such as the Ca II triplet (PP1). The high-velocity line peaks are typically blueshifted by $\gtrsim$100 km s^{-1} with respect to the star and the centroids of the permitted lines. The low-velocity peaks can be blueshifted as much as 50 km s^{-1} (in DG Tau) with wings extending to positive velocities.

The high- and low-velocity blueshifted components usually appear together. Clear examples of this are the double-peaked blueshifted profiles of RU Lup, VV CrA, and DG Tau. The correlated presence of these two velocity components suggests that the low-velocity emission is not related to the narrow rest-velocity lines discussed above. In sources without multiple peaks, such as S CrA, R Mon, and V536 Aql, the division between high and low velocities is uncertain, but the distinct nature of the components is clear from their different relative strengths in different lines. For example, the data show that [N II] and [O II] are *always* relatively stronger and [O I] λ5577 is *always* relatively weaker at high velocities (Edwards et al. 1989; and § 4.3 below).

Two sources, RW Aur and AS 353A, have emission peaks at high redshifted velocities $\gtrsim$100 km s^{-1}. In [O I] λ6300 these peaks have blueshifted counterparts at similar (but not identical) negative velocities.

Figure 3 shows the relationship between the [O I] λ6300 and Hα and Ca II λ8542 equivalent widths. Figure 3*a* is similar to the plot in Cabrit et al. (1990) showing a weak correlation between Hα and the total [O I] line strengths. Figure 3*b* shows a similar *weak* correlation with the Ca II triplet. Figures 3*c* and 3*d* plot the high-velocity components of [O I] against the total strengths of the two permitted lines. The [O I] measurements are from Tables 1–5. For Figures 3*c* and 3*d*, the red- and blueshifted emissions of RW Aur and AS 353A are added together, the high-velocity [O I] in RY Tau is estimated at $\sim$40% of the total, and CW Tau, V536 Aql, KK Oph, and R CrA are excluded, in spite of their having clear high-velocity components, because their profiles are not easily divided into velocity intervals. These panels show that the high-velocity [O I] is *usually* stronger in sources with strong permitted lines. The most notable exceptions, having no detectable high-velocity [O I], are Haro 1-1, with W_λ(Hα) $\approx$ 105 Å, and CV Cha and V380 Ori, with W_λ (8542) $\approx$ 11 and 20 Å, respectively.

4.2.2. *Jets and Multiple Wind Components*

Spectral imaging results (e.g., Solf 1989; Solf & Böhm 1993) show that the blueshifted high-velocity regions in DG Tau and HL Tau are spatially separate from the low-velocity gas, stratified in terms of their line ratios and thus physical conditions, and probably associated with extended jets. If the lines form

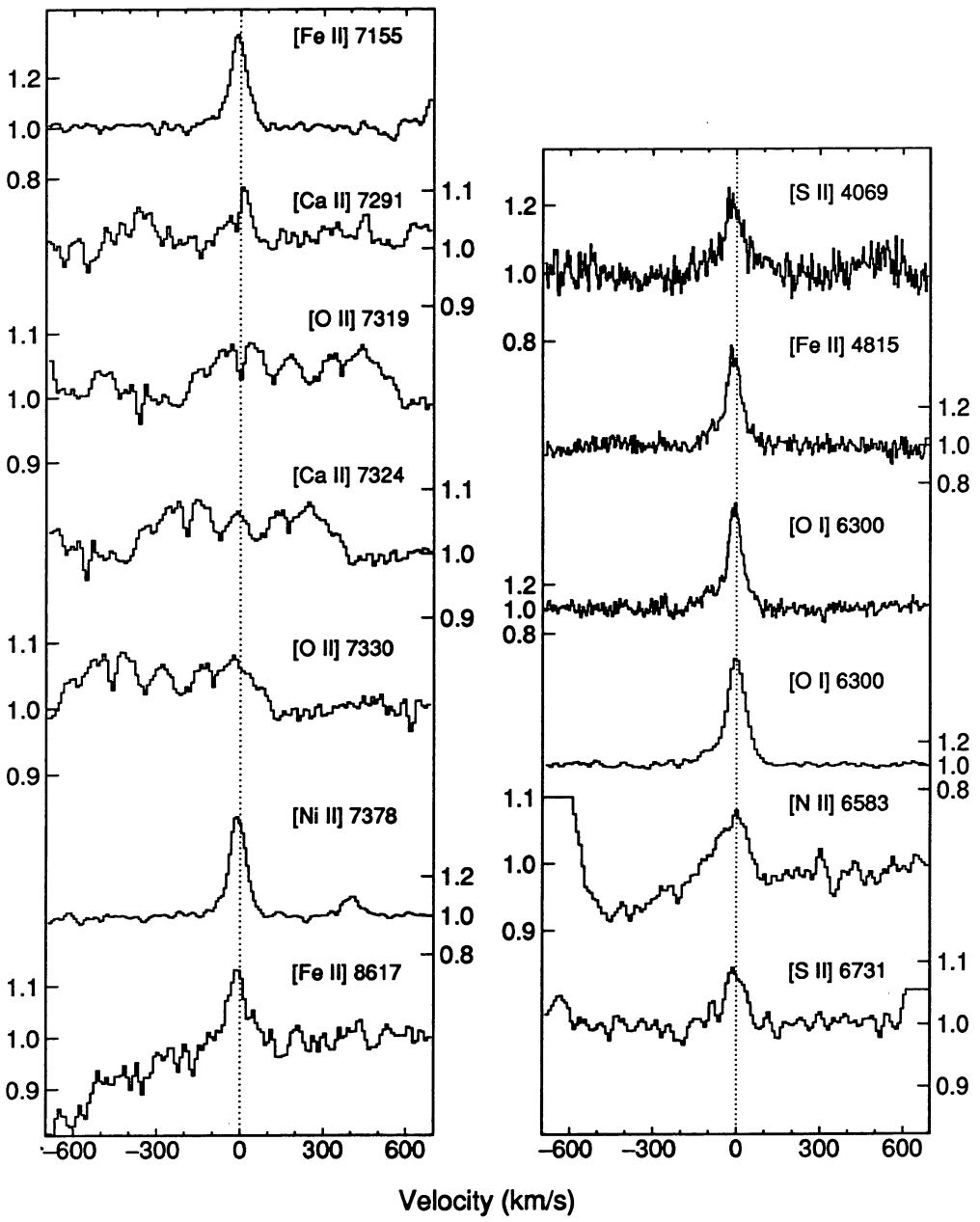

FIG. 2a—KK Oph

FIG. 2.—(*a*) KK Oph: 1989 April. The rest velocity, $V_* \approx 10$ km s^{-1}, is adopted from Finkenzeller (1985). [Ca II] λ7324 and the two [O II] lines are blended. See also information for Figs. 1*a*–1*c*. (*b*) R CrA: 1989 April. The velocities are heliocentric. The permitted Ca II lines are shown after subtracting the blended Paschen lines, although some residual Paschen emission remains on the red side of both Ca II profiles in the figure. See PP1 and information for Figs. 1*a*–1*c*. (*c*) PV Cep: 1988 September. The velocities are heliocentric. See information for Fig. 1*a*. (*d*) LkHα 233: 1988 September. The velocities are heliocentric. See information for Fig. 1*a*. (*e*) R Mon. The [N II] and [S II] were measured in 1983 December. All others are from 1987 December. The velocities are heliocentric. See information for Fig. 1*a*.

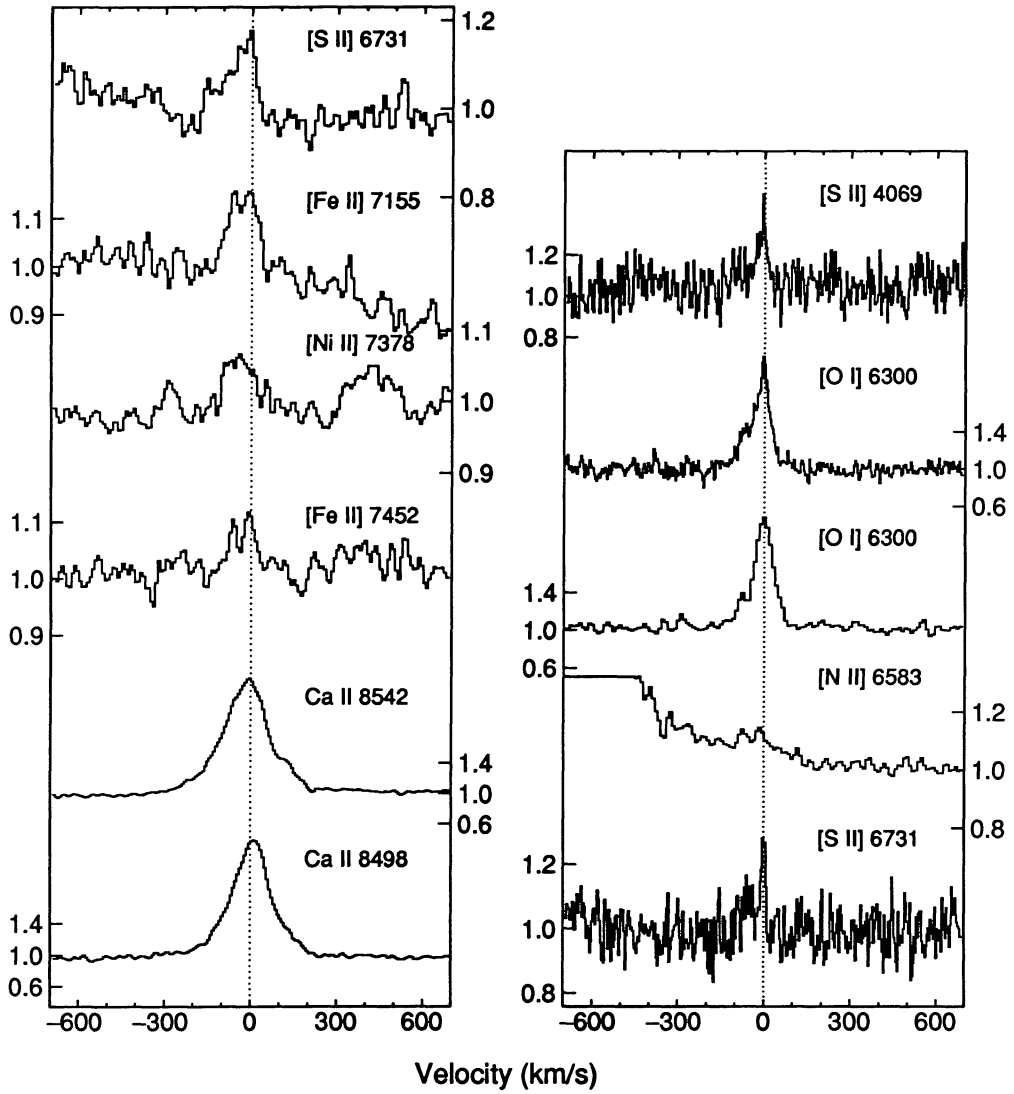

FIG. 2*b*—R CrA

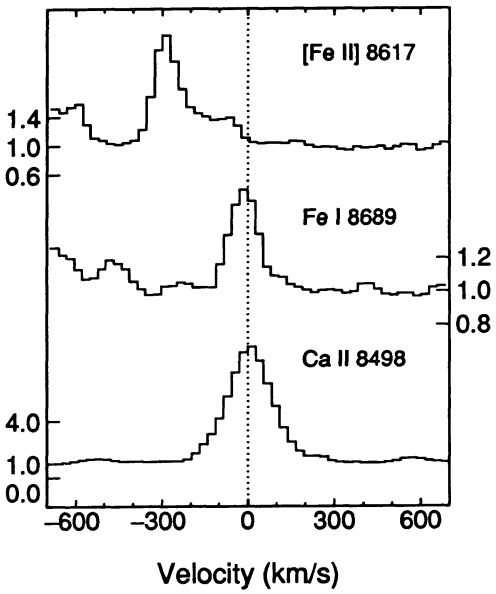

FIG. 2*c*—PV Cep

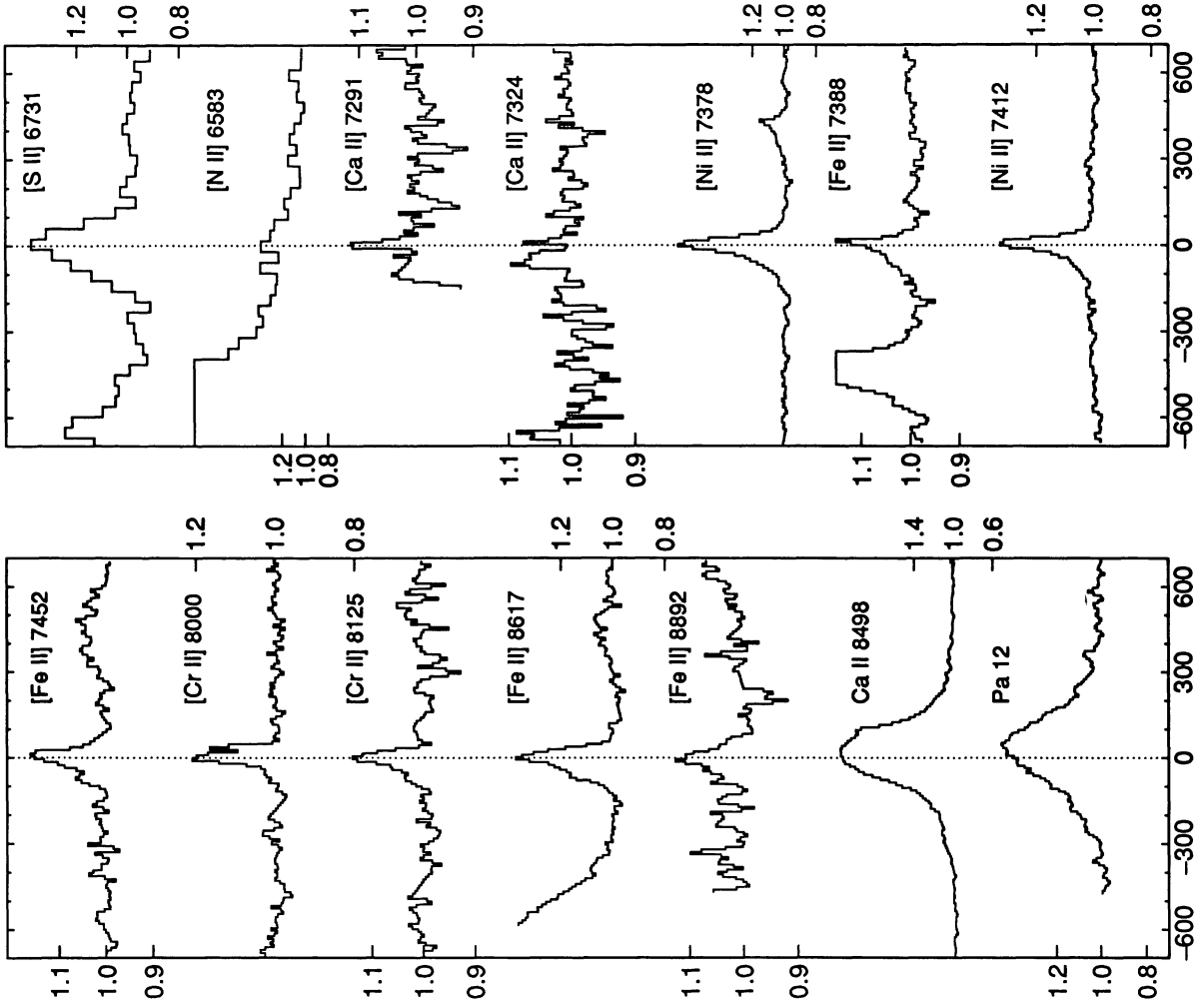

FIG. 2*e*—R Mon

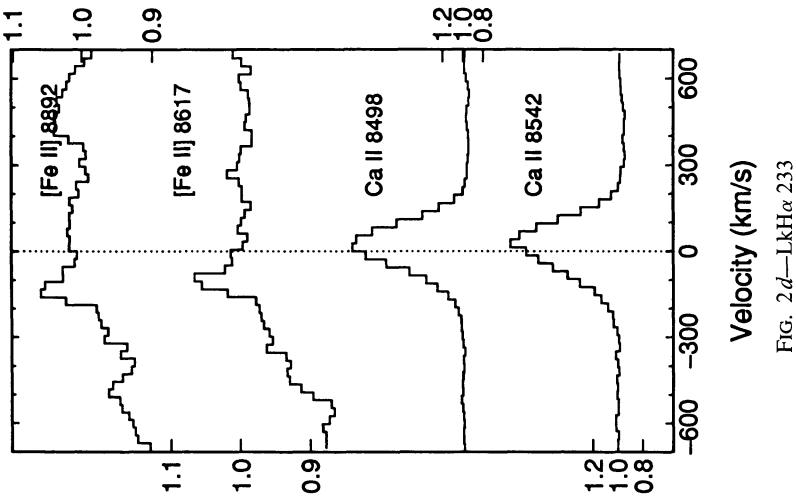

FIG. 2*d*—LkHα 233

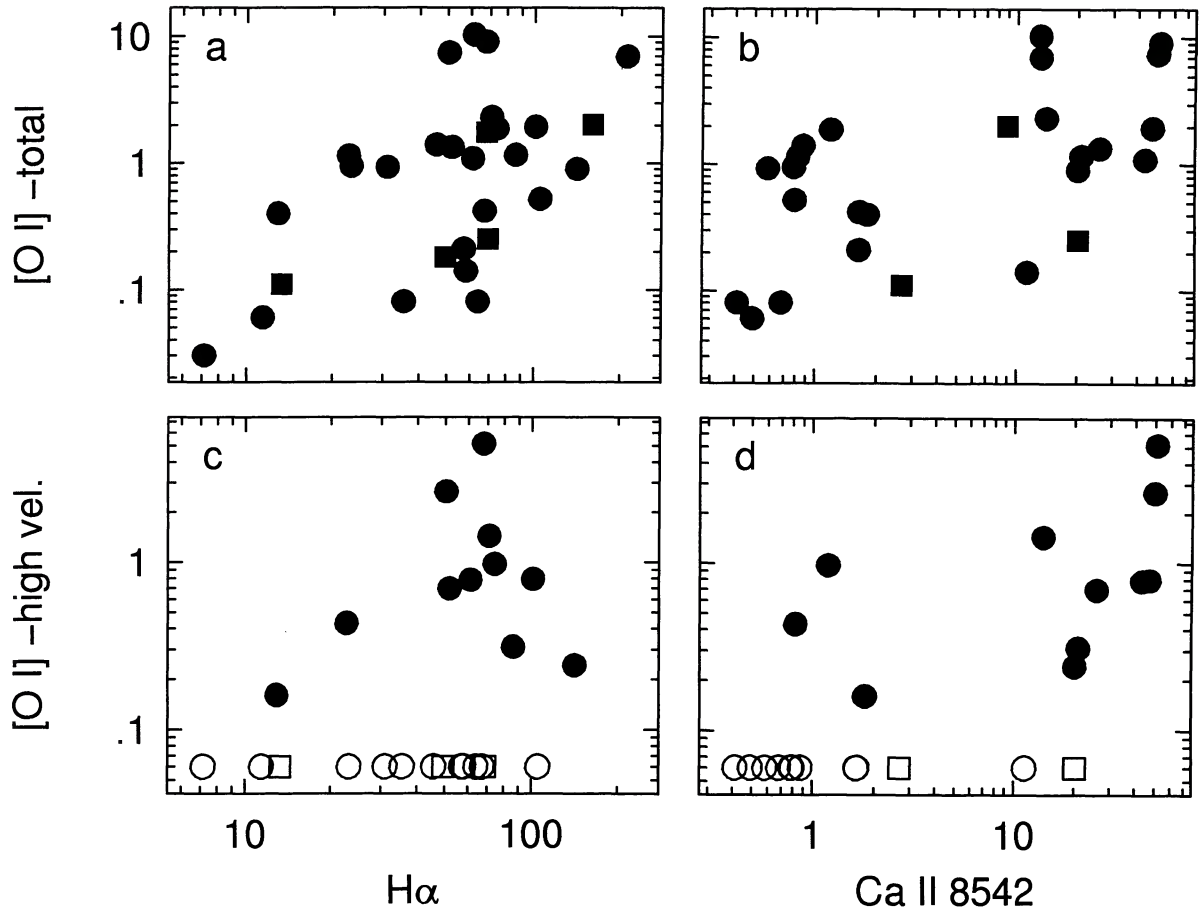

FIG. 3.—(*a*) and (*b*) Comparison of the total equivalent widths (in angstroms) in [O I] λ6300 to those in Hα and Ca II λ8542. (*c*) and (*d*) Comparison of just the high-velocity [O I] (from Tables 2 and 3) to the total Hα and Ca II equivalent widths. The circles and squares represent TTSs and Herbig Ae–Be stars, respectively. The open symbols at the bottom of (*c*) and (*d*) indicate approximate upper limits to the high-velocity [O I] strengths. See § 4.2.1.

generally in jets, the degree of collimation is constrained by the profiles. The important parameter is the ratio of line width to centroid velocity: FWHM/V_c. Narrow lines at high velocity, i.e., small FWHM/V_c, require well-collimated jets. Kwan & Tademaru (1988) calculated line profiles for conical winds with a range of opening angles and orientations. In the present data, the [Ca II] lines of DG Tau and HL Tau, where FWHM/$V_c \sim 0.18$, require the smallest full angles of $\lesssim 20°$. Possible velocity gradients in the jet make this a conservative upper limit. In RW Aur and AS 353A the blue- and redshifted peaks could form in oppositely directed jets. The distinct redshifted peaks in the [S II] lines of RW Aur would require opening angles $\lesssim 60°$.

Different line widths in the same source sometimes indicate a range of opening angles or velocity dispersions across the emitting regions. For example, in S CrA and VV CrA the high-velocity peaks in [S II] λ6731 and [N II] λ6583 are considerably sharper than in [O I] and other lines. In DG Tau the blue-shifted [Ca II] lines are *much* narrower than the other features. The changing profiles in DG Tau also suggest that the degree of collimation or velocity coherence can vary on timescales of a few years.

4.3. *Density, Temperature, and Ionization across the Profiles*

In this section, the physical conditions in the emitting regions are estimated by comparing the line ratios in Tables 2–5 to those calculated in the Appendix. The discussion involves both the total line strengths and the differences between the high- and low-velocity intervals defined in §§ 3.1 and 4.2.1. The theoretical ratios within a given ion assume that the lines are collisionally excited by free electrons at well-defined densities and temperatures. Comparing lines of different ions invokes the additional assumptions of solar abundances and coronal ionization equilibrium. These collisionally dominated calculations provide a good first approximation to the (probably) shock-excited FELRs in young stars (also Gomez de Castro & Pudritz 1993). Realistic shock environments can include a range of temperatures and densities where the gas cools and radiates. The spectral imaging observations (Solf 1989; Solf & Böhm 1993) of spatially segregated emitting regions imply that a range of conditions do, in fact, obtain in the FELRs. In this circumstance, each line forms under the conditions that most favor its emission. Therefore the physical conditions are estimated below separately for several important

lines. The main results are summarized in Table 6, where the column heads "high" and "low" refer to the blueshifted velocity intervals (§§ 3.1 and 4.2.1) and f is the ionization fraction of H.

4.3.1. [O I]

The various line strengths compared to λ6300 imply $T_e \lesssim$ 14,000 K in the [O I] region (Fig. 5). At higher temperatures [N II] λ6583 and [S II] λ6716 would be too strong at low densities and [O II] λ7319 and [S II] λ4069 too strong at high densities. If all the lines formed in the same region, $T_e \lesssim$ 11,000 K could be ruled out for most sources because the singly ionized lines (e.g., [S II] λ6731) would be too weak compared to [O I] λ6300. However, § 4.3.3 will show that [N II], [O II], and at least some of the [S II] form in a hotter environment. Therefore, lower T_e's might be present in the [O I] region. The lower limit is probably ~9000 K, otherwise the values of n_e inferred from λ5577/λ6300 (below) would require extremely large hydrogen densities (n_H) in the mostly neutral gas (see the Appendix). Because the higher ionization lines form partly in a separate environment, the upper limit of 14,000 K in the [O I] zone is conservatively high. For $T_e < 14{,}000$ K the gas is mostly neutral, with H^+ fractions <35% (Fig. 4).

The ratio [O I] λ5577/λ6300 provides a diagnostic of the persistent differences between the high- and low-velocity intervals. In particular, λ5577 is never clearly detected at high velocities. Emission from λ5577 is favored at both higher densities and higher temperatures (Fig. 6). For a fixed n_e, different T_e's could account for the changes in λ5577/λ6300 only if the gas is dramatically cooler at high velocities. However, the [N II] and [O II] lines imply that there are *higher* temperatures at high velocities (below). Therefore the weakness of λ5577 at high velocities is probably due to lower n_e's, as suggested by Edwards et al. (1989). For $T_e \sim$ 11,000 K, the firmest upper limits on λ5577 at high velocities imply $n_e \lesssim 5 \times 10^5$ cm^{-3}. At low velocities the measured ratios and upper limits imply n_e from $\lesssim 10^6$ cm^{-3} to $\sim 10^7$ cm^{-3}. A good example of the n_e velocity dependence is DF Tau, where the measurements imply $n_e \lesssim 5 \times 10^5$ cm^{-3} at high velocities and $\sim 10^7$ cm^{-3} at low velocities (for $T_e \sim$ 11,000 K).

4.3.2. [S II]

The ratio [S II] λ6716/λ6731 is a well-known density diagnostic that has no temperature dependence (Fig. 7; Osterbrock 1989). Most of the observed λ6716/λ6731 ratios are consistent, within the uncertainties, with saturation at $n_e \gtrsim 5 \times 10^3$ cm^{-3}. The only clear exceptions are HL Tau, whose [S II] lines suggest $n_e \sim 10^3$ cm^{-3} (although the signal-to-noise ratio is poor), and RW Aur, whose unusual redshifted lines are discussed below. There is no clear evidence in this ratio for differences between the high- and low-velocity intervals.

[S II] λ4069 is another useful diagnostic (Fig. 7), although ratios involving this line are much more sensitive to uncertainties in the extinction and continuum calibration (§ 2). The errors could easily exceed a factor of 2 for the "well-veiled" and highly variable sources considered here (see PP3; Basri & Batalha 1990). Nonetheless, the extinction-corrected ratios λ4069/λ6731 suggest n_e between $\sim 1 \times 10^4$ and $\sim 7 \times 10^4$ cm^{-3}. The strength of λ4069 relative to other ions suggests $T_e \gtrsim$ 13,000 K (Fig. 5). Independent of the calibration uncertainties, the similar λ4069 and λ6731 profiles in S CrA indicate no change in the physical conditions with velocity. However, in RU Lup the different profiles indicate higher T_e (or possibly n_e) in the high-velocity [S II] region. The high-velocity λ4069 flux was not measured in other sources because of severe blending with Fe I λ4063.

For any density in the [S II] λ6731 zone, $T_e \gtrsim$ 11,000 K is required to keep the relative flux in [O I] λ6300 at or below most of the observed values. Spectral imaging shows that the [O I] forms mostly outside the [S II] region at high velocities in DG Tau and HL Tau (Solf 1989; Solf & Böhm 1993). The different densities derived from [O I] and [S II] at low velocity (above) also imply different emitting regions. Therefore [O I] emission from the [S II] region is minimal at all velocities, and the lower limit on T_e in the [S II] zone is probably closer to ~13,000 K. The upper limit on T_e follows from the relative strength of [O II]. For $n_e \gtrsim 5 \times 10^3$ cm^{-3}, the few [O II] measurements imply $T_e \lesssim$ 18,000 K at high velocities and ≲14,500 K at low velocities. Note that upper limits on T_e derived from [N II]/[S II] are a few thousand kelvin less than these [O II] results. (At the T_e's just discussed, the predicted flux in [N II] λ6583 at low velocities is somewhat larger than observed. This discrepancy can be understood if the N^+ fraction is too large in the present calculations; see the Appendix.)

4.3.3. [N II] *and* [O II]

Another persistent trend in the profiles is that [N II] and [O II] are always stronger at high velocities compared to [O I], [S II], and most other lines. In some sources, such as RU Lup, VV CrA, CW Tau, and DG Tau, the [N II] and [O II] (if

TABLE 6

ESTIMATED PHYSICAL PARAMETERS

Parameter	[O I] "high"	[O I] "low"	[S II] "high"	[S II] "low"	[N II], [O II] "high"
T_e (K)	~9000–14000		~13000–18000	~13000–14500	~15000–35000
f	35%		...		≳50%
n_e (cm^{-3})	≲5 × 10^5 (assuming $T_e \sim$ 11000 K)	≲10^6–10^7	~10^3–10^5		≲10^5

present) are exclusively at high velocities. Even in sources with relatively narrow single-peaked lines, such as V536 Aql and XZ Tau, the [N II] and [O II] are more blueshifted than other lines. In KK Oph, where all of the line peaks are at low velocity, [N II] and [O II] have stronger blueshifted wings.

This trend in [N II] and [O II] cannot result simply from lower densities at high velocities because that would strengthen [S II] λ6731 even more than [N II] (Fig. 5). Also, lower densities would weaken [O II] instead of making it stronger. Strong [N II] λ6583 does require low densities, but higher temperatures must be the main reason [N II] and [O II] are stronger.

In principle, one could derive temperatures from the [O II]/[O I] line ratios, with the general result that T_e is larger at high velocity. However, that temperature estimate, and even the sense of the temperature difference with velocity, cannot apply to all of the emitting regions. Different line ratios in the same source can yield different results, and changes in the ratios with velocity can suggest contradictory changes in the parameters. For example, in DG Tau and VV CrA the [S II] λ6731 profile has less flux at high velocities and less flux relative to [O I] λ6300. The models would predict the opposite if T_e were uniformly larger, or n_e uniformly smaller, at high velocities. The data for RU Lup show that the contradictions can also appear in the density diagnostics. In particular, [S II] λ4069/λ6731 implies higher n_e at high velocities, while [O I] λ5577/λ6300 implies the opposite.

These *apparent* conflicts only show that the various lines do not form in the same gas. The conflicting T_e estimates for DG Tau and VV CrA are resolved if the blueshifted [N II] and [O II] lines form in a hot environment that emits mostly in these lines. The weakness of [N II] and [O II] at low velocities implies that the hot gas is not a factor there. The densities in the hot region must be $\lesssim 10^5$ cm^{-3} to insure that [N II] λ6583 is strong and [O II] is not much stronger than [N II] (Fig. 5). Measurements of the density-sensitive doublet [O II] λ3726 and λ3729 would be helpful. The models predict that λ3726 should have ~ 1 to $\gtrsim 10$ times the flux of λ7319 for $N_e \lesssim 10^5$ cm^{-3} (Fig. 7.)

If cooler gas from another region contributes most of the [O I], the [O II]/[O I] line ratio is *not* a valid measure of T_e in the [O II] zone. The ratio provides only a lower limit on T_e. The most reliably measured [O II]/[O I] ratio in DG Tau implies $T_e \gtrsim 14{,}000$ K at high velocities. More generally, the temperature in the hot region is constrained by the requirement that [N II] and [O II] are both strong compared to [O I]. This suggests $T_e \gtrsim 15{,}000$ K if $n_e \lesssim 10^5$ cm^{-3}. The corresponding limit on the ionization fraction is $\gtrsim 50\%$. With the present data, the upper limit on T_e is constrained only by the requirement that higher ionization lines, such as [O III] λ5007, [S III] λ9069, and [Ar III] λ7136, are weak compared to [N II] and [O II]. This implies $T_e \lesssim 35{,}000$ K according to the models (not shown).

4.3.4. [C I], [Ca II], *and Dust in the FELR*

For solar abundances and any of the densities and temperatures derived above, [C I] λ8727 and [Ca II] λ7291 should have $\gtrsim 0.2$ and $\gtrsim 0.4$ times the strength of [O I] λ6300, respectively (Fig. 5). The measured ratios and upper limits are always smaller for [C I] and usually smaller for [Ca II]. This suggests that the C and Ca abundances are depleted by dust grains in the line-forming regions. In the interstellar medium, C and Ca are expected to be depleted by factors of a few and >10, respectively, compared to solar ratios (Cowie & Songaila 1986). Thus the predicted ratios for [C I] and [Ca II] are probably too large by the same factors. AS 353A, RW Aur, and V380 Ori have [Ca II] strengths within the predicted range, implying that they *do not* have significant dust depletions. Their broad [Ca II] lines are centered at the stellar/permitted-line velocities, and, while strong compared to [O I], they have just $\sim 1\%$ of the flux in the Ca II infrared triplet. Their [Ca II] lines could form in the permitted-line region at densities $\gtrsim 10^{11}$ cm^{-3} (PP1; PP2). This dense and probably turbulent environment near the star is very different from the nominal FELR and could well be dust free.

4.3.5. *AS 353A and RW Aur*

The multiple line peaks in AS 353A and RW Aur deserve special attention. In AS 353A the [O I] λ5577/λ6300 ratios imply densities of several times 10^6 cm^{-3} at low velocities, and probably lower densities in the high-velocity intervals. In RW Aur, the ratio of redshifted [S II] λ6716/λ6731 implies $n_e \sim 10^3$ cm^{-3}. The absence of these lines at other velocities, where [O I] remains strong, is probably due to higher densities (Fig. 5). The detection of strong [S II] λ4069 at the "central" velocity implies that higher densities do occur. For any density, the ratio of redshifted λ6731/λ6300 suggests $T_e \gtrsim 13{,}500$ K in the [S II] region, but the weakness of [N II] λ6583 compared to λ6731 suggests $T_e \lesssim 11{,}000$ K. This apparent contradiction cannot be reconciled by invoking a cool [O I] region or a hot [N II] region, but it can be understood if the N^+ fraction is too large in the calculations (see the Appendix and the end of § 4.3.5.).

5. SUMMARY AND CONCLUSIONS

Forbidden-line data are discussed for 42 pre–main-sequence stars. The lines range in ionization from [C I] and [O I] to [N II] and [O II]. Profile variability occurred in DG Tau and perhaps other sources. The ensemble of complex profiles can be divided into four common components: (1) narrow rest-velocity lines, (2) low-velocity line peaks or wings, (3) high-velocity blueshifted peaks or wings, and (4) high-velocity redshifted peaks. The rest-velocity lines are narrow and roughly symmetric about zero velocity. The low-velocity emission peaks at $\lesssim 50$ km s^{-1}, while the high-velocity flux is usually at $\gtrsim 100$ km s^{-1}. These four components may generically identify distinct emitting regions in young star envelopes. Among TTSs, the rest-velocity lines appear more often in sources with weak and narrow permitted lines, such as the Ca II triplet. The high- and low-velocity blueshifted components usually appear together in sources with strong and broad Ca II triplet lines.

Different profiles in the same spectrum imply that the physical conditions vary with velocity across the profiles. The most persistent trends are for more [N II] and [O II] and less [O I] λ5577 flux at high velocities. The line ratios are examined in the high- and low-velocity intervals to estimate the density, temperature, and ionization of the gas. This analysis uses models of multilevel ions in coronal ionization equilibrium. The main results are summarized in Table 6. Both the high- and

low-velocity intervals can have considerable flux from [O I] and [S II]. In the [O I] zone, densities range from $n_e \lesssim 5 \times 10^5$ to $\sim 10^7$ cm^{-3}, but $n_e \gtrsim 10^6$ cm^{-3} obtains only at low velocities. The temperatures are in the range $9000 \lesssim T_e < 14{,}000$ K, and the ionization fraction (of H^+) is <35%. The [S II] region requires strictly lower densities, with estimates between $10^3 \lesssim n_e \lesssim 7 \times 10^4$ cm^{-3}. The temperature in the [S II] gas is $\gtrsim$13,000 K. At high velocities (only) there is an additional hot environment that produces [N II] and [O II], at least some of the [S II], and little [O I]. This region is characterized by $n_e \lesssim 10^5$ cm^{-3}, $T_e \gtrsim 15{,}000$ K, and an ionization fraction $\gtrsim$50%. Measurements of the [O II] λ3729/λ3726 ratio would help define the density in this hot gas. Note that differences of several decades in n_e between the [O I] and [S II] and [N II] regions imply differences *at least* that large in the gas density (n_H) because the [O I] zone is more neutral.

Spectral imaging of DG Tau and HL Tau has shown that at high velocities [O I] λ6300 forms closer to the star than do [S II] λ6731 and [N II] λ6583 (Solf 1989; Solf & Böhm 1993). Those results imply that the high-velocity lines form in jets with radially decreasing density. The present work shows that the [N II] and [O II] are also associated with higher temperatures. Therefore the [O I], [S II], [N II], and [O II] lines probably trace, in order, a decrease in n_e *and* an increase in T_e away from the stars.

If the high-velocity lines do form in jets, the line profiles constrain the opening angle of the flow. The smallest (full) opening angles are $\lesssim$20° implied by the [Ca II] lines of DG Tau and HL Tau. Other broader lines at the same velocity in these objects imply less collimated flows or larger velocity dispersions. For example, the broader [O I] compared to [S II] and [Ca II] at high velocities, in DG Tau, HL Tau, and S CrA, and VV CrA, is consistent with poorer collimation in the cooler gas near the star (Solf 1989; Solf & Böhm 1993). The profile variability in DG Tau also shows that the opening angles or velocity dispersions in a given line-forming region can change in less than a few years. In RW Aur and AS 353A the blue and redshifted peaks in [O I] suggest oppositely directed jets. The exclusively redshifted [S II] lines in RW Aur require opening angles $\lesssim$60°.

I am grateful to G. J. Ferland for invaluable help in running his spectral synthesis code CLOUDY, and to S. E. Persson for his collaboration on the observations at the Palomar and Las Campanas observatories. P. J. McGregor and S. E. Persson also generously provided the 1983 spectra measured at Palomar. M. Simon and a referee provided helpful comments on this manuscript. I also thank J. McCarthy for his instruction in the use of the echelle spectrometer at Palomar, P. L. Schechter and S. A. Shectman for their help with the instrumentation at Las Campanas, and the staffs of the Palomar, Kitt Peak, and Las Campanas observatories for their willing assistance during the observations. My research is supported by NASA grants NAG 5-1645 and NAG 5-1630 and by a Columbus Fellowship at The Ohio State University. This work used the SIMBAD database, operated by the Centre de Données Stellaires, Strasbourg.

APPENDIX
THEORETICAL LINE RATIOS

In this appendix the ionization and emission-line ratios are derived for gas in "coronal ionization equilibrium" at various densities and temperatures. The calculations use the spectral synthesis code CLOUDY, most recently described by Ferland (1993). The ionization equilibrium is dominated by electron collisions and charge exchange reactions. At high densities and low temperatures, collisions with neutral atoms can also influence the ionization (see below). The line strengths are derived by solving the detailed balance equations for multilevel ions. The forbidden lines are excited by electron impacts. The lines (permitted and forbidden) and the continuum at all wavelengths are assumed to be optically thin. There are no external radiation fields. The diffuse radiation from the gas is included but not important. The elemental abundances are solar (from Grevesse & Anders 1989).

Figure 4 shows the ionization fractions for several elements as a function of the equilibrium temperature. The results are not sensitive to the density and are plotted for a total hydrogen density ($H^0 + H^+$) of $n_H = 10^5$ cm^{-3}. As the gas becomes more ionized from left to right in the figure, the free electron density n_e increases from $\sim$5 cm^{-3} at $T_e = 7000$ K to $\sim 10^5$ cm^{-3} at 20,000 K. Some of the results in Figure 4 differ from previous estimates of ionization equilibrium (Shull & Van Steenberg 1982; Arnaud & Rothenflug 1985) because of the more extensive treatment of charge exchange, the inclusion of collisional ionization by neutral atoms (H^0), and the sometimes different reaction cross sections used in CLOUDY. For example, the ionization temperature of N^0 is $\sim$1300 K lower in Figure 4 because of charge transfer ionization and recombination reactions with H (see also Osterbrock 1989). The Ni^+ fraction is higher at high temperatures because of efficient charge exchange recombination of Ni^{++} reacting with H^0. The appearance of significant Ca^{++} and S^{++} inside the Ca^0 and S^0 zones, at $\sim$8000 K and $\sim$11,000 K, respectively, is caused by collisional ionization with neutral atoms in a gas where the scarcity of free electrons inhibits recombination. As n_e grows with higher temperatures, Ca^{++} and S^{++} become suppressed until collisional ionization by electrons becomes important.

Figure 5 shows the strength of various lines relative to [O I] λ6300 at six temperatures. The line ratios are plotted as a function of n_e. The true gas density can be decades larger if the gas is mostly neutral. In particular, $n_H/n_e \approx 1400$ at $T_e = 9000$ K, $\sim$60 at 11,000 K, $\sim$6.4 at 13,000 K, $\sim$1.9 at 15,000 K, and $\sim$1.0 at 22,000 K (see also Fig. 4). The lines plotted are the strongest forbidden lines predicted by the models at the observed wavelengths. The only line not shown is [Ar III] λ7135, which would appear in just the $T_e =$ 22,000 K plot with relative flux 0.21 at $n_e = 10^2$ cm^{-3} and 1.5 at 10^8 cm^{-3}. The models do not predict fluxes for [Cr II], [Fe II], [Fe III], or [Ni II]. Note that the vertical positions of the curves, but not their shapes, change significantly with the temperature. The vertical positions are roughly commensurate with the ionization (Fig. 4). For example, lowering the N^+ fraction—to be more like the previous estimates (above)—would weaken the predicted [N II] fluxes shown in Figure 5. The shapes of the curves in Figure 5 can be understood in terms of the critical electron densities, n_{cr}, where the line upper states are deexcited equally by collisions and radiative decays. The critical density of [O I] λ6300 is $\sim 10^6$ cm^{-3}. The relative decline in [N I] λ5200, [N II] λ6583, and [S II] λ6731

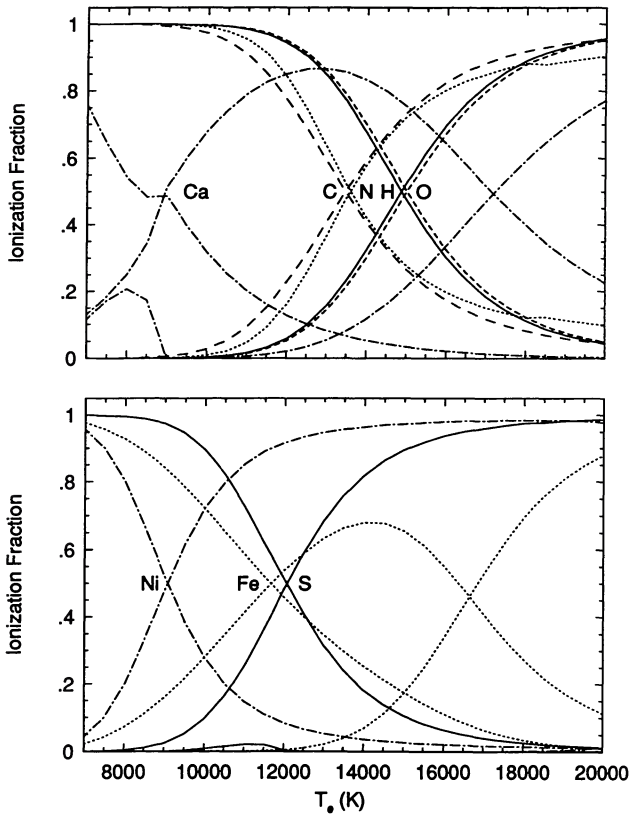

FIG. 4.—Ionization fractions of several elements are plotted as functions of the electron temperature T_e for gas in coronal equilibrium at a constant hydrogen ($H^0 + H^+$) density of $n_H = 10^5$ cm^{-3}. Each element is represented by a different line type. Several ionization stages are shown for each element. The curves are labeled at the first ionization boundary, where the falling neutral fraction intersects the rising first ion fraction. At higher temperatures, the rising curves for Ca and Fe represent Ca^{++} and Fe^{++}, respectively. The curves for S^{++} and Ca^{++} have local maxima at temperatures just below the first ionization edges, at ~11,000 K for S^{++} and ~8000 K for Ca^{++}.

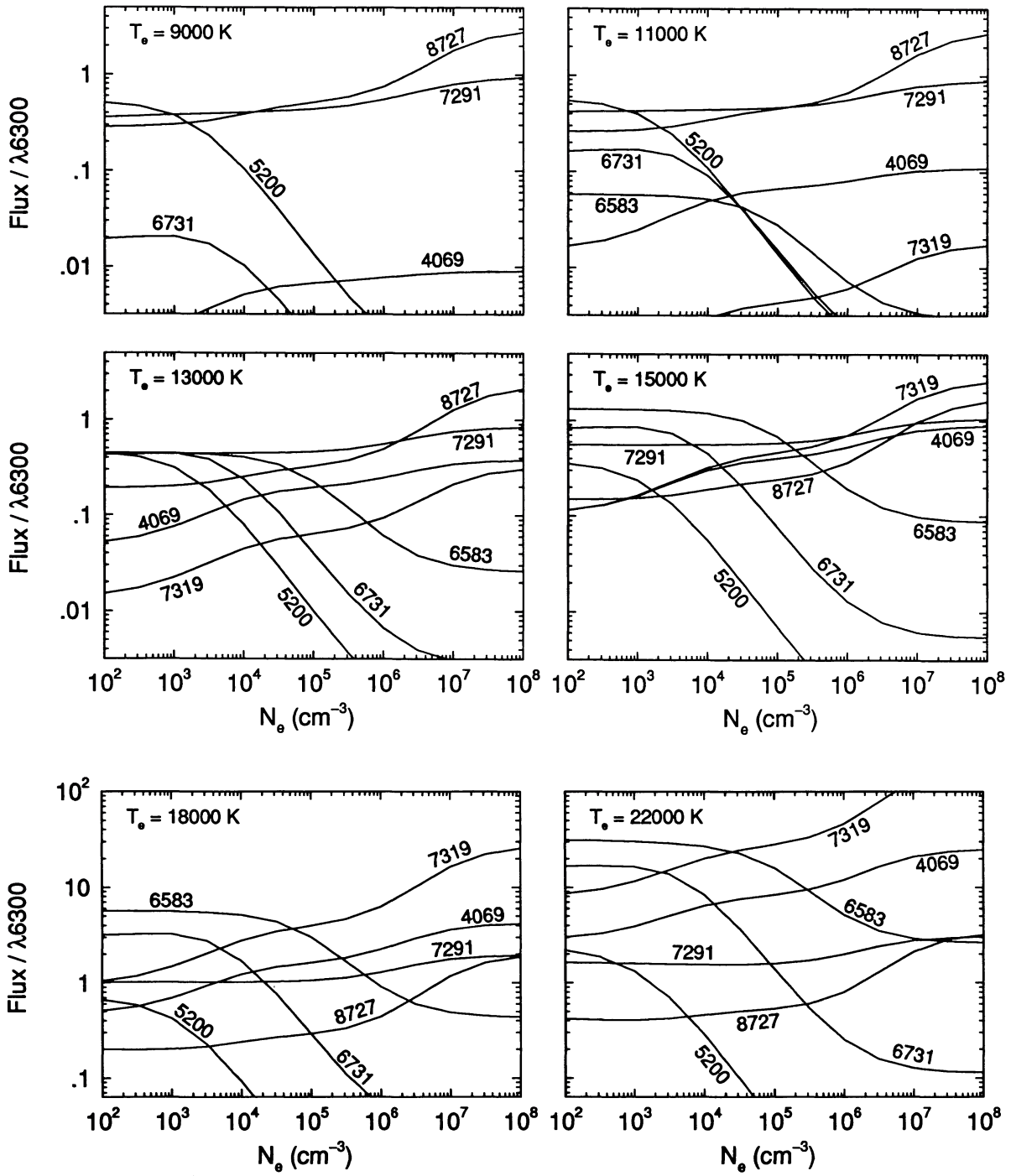

FIG. 5.—Line strengths relative to [O I] λ6300 are plotted against electron density for six temperatures labeled in the upper left of each panel. Note the change in vertical scale in the bottom two panels. The lines are "5200" = the sum of the [N I] multiplet near 5200 Å, "7319" = the sum of the [O II] doublet near 7319 Å (does not include the ~7330 Å pair). The rest are single lines, "8727" = [C I] λ8727, "6583" = [N II], "6731" = [S II], "4069" = [S II], and "7291" = [Ca II].

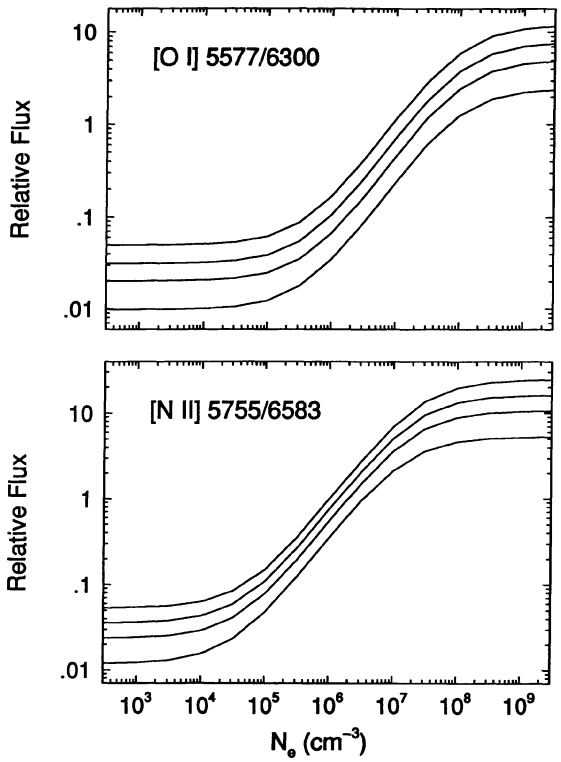

FIG. 6.—Line ratios of [O I] and [N II] are plotted against electron density for the temperatures, T_e = 9000, 12,000, 15,000, and 20,000 K, with T_e increasing from bottom to top.

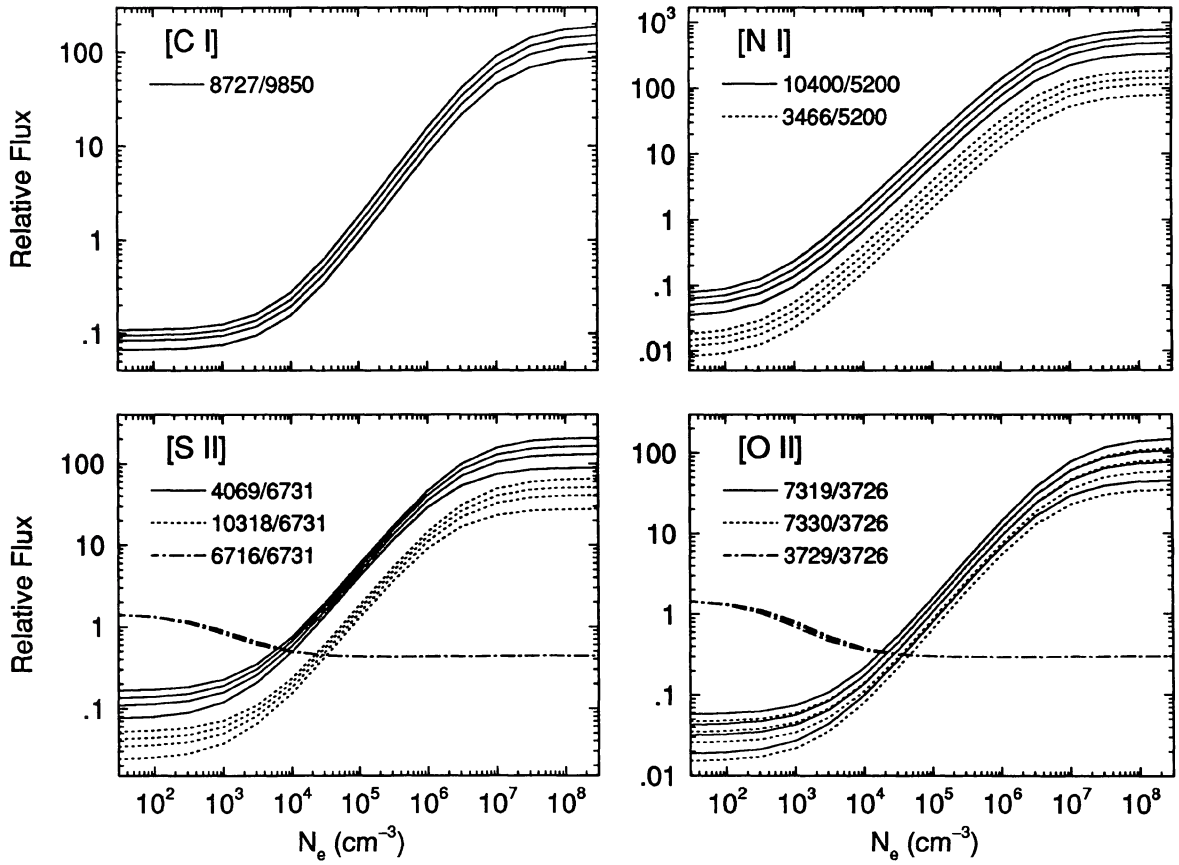

FIG. 7.—Line ratios of [C I], [N I], [S II], and [O II] are plotted against electron density for the temperatures, T_e = 9000, 12,000, 15,000, and 20,000 K, with T_e increasing from bottom to top. [O II] λ7319 and [N I] λ5200 and λ10400 represent the summed flux in these multiplets (see Fig. 5 caption).

toward high densities occurs because these lines are collisionally suppressed for $n_e \gtrsim 10^4$ cm^{-3}. The [C I] λ8727, [O II] λ7319, [S II] λ4069, and [Ca II] λ7291 ratios rise toward higher densities because their upper states have $n_{cr} > 10^6$ cm^{-3}.

Forbidden line ratios within a given ion depend only on n_e and T_e and not on the ionization state or the assumptions of coronal equilibrium. Figure 6 shows the ratios [O I] λ5577/λ6300 and [N II] λ5755/6583 at four temperatures, 9000, 12,000, 15,000, and 20,000 K. Emission from λ5577 is favored at high densities and temperatures because it has a larger critical density, $\sim 10^8$ cm^{-3}, and roughly double the excitation energy, 4.2 eV compared to 2.0 eV for λ6300. The [N II] ratio is analogous but the lines have roughly a decade lower critical densities. Figure 7 shows the similar behaviors for line ratios of [C I], [N I], [S II], and [O II]. [S II] λ6716/λ6731 and [O II] λ3726/λ3729 in this figure are well-known density diagnostics with no dependence on T_e (Osterbrock 1989). The other line ratios are also not sensitive to the temperature, for T_e within the range of interest.

REFERENCES

Appenzeller, I., Jankovics, I., & Östreicher, R. 1984, A&A, 141, 108
Arnaud, M., & Rothenflug, R. 1985, A&AS, 60, 425
Bashkin, S., & Stoner, J. O., Jr. 1978, Atomic Energy Levels and Grotrian Diagrams, Vol. 2 (New York: Elsevier)
Basri, G., & Batalha, C. 1990, ApJ, 363, 654
Basri, G., & Bertout, C. 1989, ApJ, 341, 340
Cabrit, S., Edwards, S., Strom, S. E., & Strom, K. M. 1990, ApJ, 354, 687
Cowie, L. L., & Songaila, A. 1986, ARA&A, 24, 499
Edwards, S., Cabrit, S., Ghandour, L. O., & Strom, S. E. 1989, in Low Mass Star Formation and Pre-Main Sequence Objects, ed. B. Reipurth, (ESO Workshop Proc. 33) (Garching: ESO), 385
Edwards, S., Cabrit, S., Strom, S. E., Heyer, I., Strom, K. M., & Anderson, E. 1987, ApJ, 321, 473
Eislöffel, J., Solf, J., & Böhm, K. H. 1990, A&A, 237, 369
Ferland, G. J. 1993, HAZY: A Brief Introduction to Cloudy, Univ. Kentucky Internal Report, in preparation
Finkenzeller, U. 1985, A&A, 151, 340
Gomez de Castro, A. I., & Pudritz, R. E. 1993, ApJ, 409, 748
Grevesse, N., & Anders, E. 1989, in Cosmic Abundances of Matter, ed. C. I. Waddington (AIP Conf. Proc. 183), 1
Hamann, F., & Persson, S. E. 1989, ApJ, 339, 1078
———. 1992a, ApJ, 394, 628 (PP3)
———. 1992b, ApJS, 82, 247 (PP1)
———. 1992c, ApJS, 82, 285 (PP2)
Hartmann, L., & Raymond, J. C. 1989, ApJ, 337, 903
Herbig, G. H. 1945, PASP, 57, 166
Hughes, J. D., Hartigan, P., Graham, J. A., Emerson, J. P., & Marang, F. 1991, AJ, 101, 1013
Jankovics, I., Appenzeller, I., & Krautter, J. 1983, PASP, 95, 883
Johansson, S. 1977, Phys. Scripta, 15, 183
Joy, A. H. 1945, ApJ, 102, 168
Kepner, J., Hartigan, P., Yang, C., & Strom, S. E. 1993, ApJ, 415, L119
Kwan, J., & Tademaru, E. 1988, ApJ, 332, L41
Moore, C. E. 1972, A Multiplet Table of Astrophysical Interest (NSRDS-NBS, vol. 40) (Washington, DC: GPO)
Mundt, R., Brugel, E. W., & Bührke, T. 1987, ApJ, 319, 275
Mundt, R., & Fried, J. W. 1983, ApJ, 274, L83
Mundt, R., Ray, T. P., Bührke, T., Raga, A. C., & Solf, J. 1990, A&A, 232, 37
Nussbaumer, H., & Storey, P. J. 1988, A&A, 193, 327
Osterbrock, D. E. 1989, Astrophysics of Gaseous Nebulae and Active Galactic Nuclei (Mill Valley, CA: University Science Books)
Raga, A. C. 1989, AJ, 98, 976
Seaton, M. J., & Osterbrock, D. E. 1957, ApJ, 125, 66
Shull, J. M., & Van Steenberg, M. 1982, ApJS, 48, 95
Solf, J. 1989, in Low Mass Star Formation and Pre-Main Sequence Objects, ed. B. Reipurth (ESO Workshop Proc. 33) (Garching: ESO), 399
Solf, J., & Böhm, K. H. 1993, ApJ, 410, L31